minerals

MDPI

Article

Petrogenesis and Geodynamic Evolution of A-Type Granite Bearing Rare Metals Mineralization in Egypt: Insights from Geochemistry and Mineral Chemistry

Mohamed M. Ghoneim [1,*], Ahmed E. Abdel Gawad [1,*], Hanaa A. El-Dokouny [2], Maher Dawoud [2], Elena G. Panova [3], Mai A. El-Lithy [2] and Abdelhalim S. Mahmoud [4]

[1] Nuclear Materials Authority, El-Maadi, Cairo P.O. Box 530, Egypt
[2] Geology Department, Faculty of Science, Menofia University, Shebin El Koum 32511, Egypt; hanaaabdelnaby4@gmail.com (H.A.E.-D.); maielleithy24@gmail.com (M.A.E.-L.)
[3] Department of Geochemistry, Saint Petersburg State University, 199034 Saint Petersburg, Russia; elena-geo@list.ru
[4] Department of Geology, Fayoum University, Al-Fayoum 63514, Egypt; halim.geologist@mail.ru
* Correspondence: moh.gho@mail.ru (M.M.G.); gawadnma@gmail.com (A.E.A.G.)

Abstract: During the Late Precambrian, the North Eastern Desert of Egypt underwent significant crustal evolution in a tectonic environment characterized by strong extension. The Neoproterozoic alkali feldspar granite found in the Homret El Gergab area is a part of the Arabian Nubian Shield and hosts significant rare metal mineralization, including thorite, uranothorite, columbite, zircon, monazite, and xenotime, as well as pyrite, rutile, and ilmenite. The geochemical characteristics of the investigated granite reveal highly fractionated peraluminous, calc–alkaline affinity, A-type granite, and post-collision geochemical signatures, which are emplaced under an extensional regime of within-plate environments. It has elevated concentrations of Rb, Zr, Ba, Y, Nb, Th, and U. The zircon saturation temperature ranges from 753 °C to 766 °C. The formation of alkali feldspar rare metal granite was affected by extreme fractionation and fluid interactions at shallow crustal levels. The continental crust underwent extension, causing the mantle and crust to rise, stretch, and become thinner. This process allows basaltic magma from the mantle to be injected into the continental crust. Heat and volatiles were transferred from these basaltic bodies to the lower continental crust. This process enriched and partially melted the materials in the lower crust. The intrusion of basaltic magma from the mantle into the lower crust led to the formation of A-type granite.

Keywords: alkali feldspar granite; geochemistry; mineral chemistry; rare metals mineralization; Egypt

Citation: Ghoneim, M.M.; Abdel Gawad, A.E.; El-Dokouny, H.A.; Dawoud, M.; Panova, E.G.; El-Lithy, M.A.; Mahmoud, A.S. Petrogenesis and Geodynamic Evolution of A-Type Granite Bearing Rare Metals Mineralization in Egypt: Insights from Geochemistry and Mineral Chemistry. *Minerals* **2024**, *14*, 583. https://doi.org/10.3390/min14060583

Academic Editor: Jaroslav Dostal

Received: 22 April 2024
Revised: 22 May 2024
Accepted: 29 May 2024
Published: 31 May 2024

1. Introduction

The Arabian Nubian Shield (ANS) is widely distributed throughout East African Orogen (EAO) and Western Arabia, including Egypt, Sudan, Ethiopia, Eritrea, Somalia, Saudi Arabia, Yemen, Oman, Jordan, and Palestine. In contrast, the southern part of the ANS is located along the Mozambique Belt (Figure 1a). The Eastern Desert of Egypt is a part of the ANS and can be subdivided into three major structural tectonic provinces, according to Stern and Hedge [1], as follows: (1) the South Eastern Desert (SED) is the oldest and most highly deformed province, and it is distinguished by the predominance of compressional and extrusion-related structures having WNW–ESE to NW–SE trends in the western part and N–S to NE–SW trends in the eastern part; (2) the Central Eastern Desert (CED) is characterized by prominent transpressional and extensional related structures having NW–SE and WNW–ESE trends, dissected by younger shearing NE–SW trend; (3) the Northern Eastern Desert (NED) is dominated by the so-called younger granite (c. 580 Ma), with extensional structures E–W and NE–SW trends. These three provinces are separated from each other by major tectonic discontinuities: the Qena–Safaga Shear Belt

between the NED and CED, and most likely, the Wadi Kharit–Wadi Hodein Shear Belt between the CED and SED. The Eastern Desert of Egypt is a part of the northern ANS [2], and it is characterized by a pronounced distribution of post- to late-collisional granites containing rare metals mineralization. This region is dated between 620 and 580 Ma [3–7].

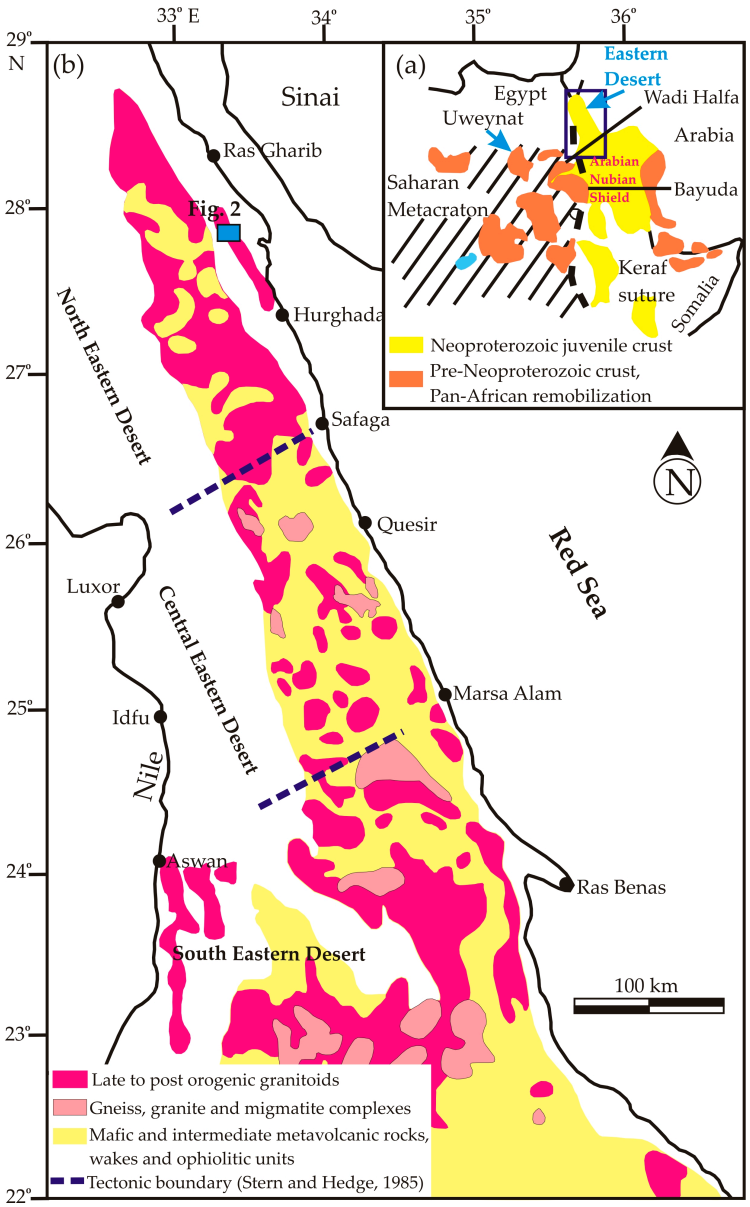

Figure 1. (**a**) Geologic map showing the Arabian Nubian Sheild (ANS). (**b**) Geological map showing the distribution of the Neoproterozoic basement rocks in the Eastern Desert, Egypt [2].

Rare metals mineralization has a markedly wide distribution in granite and associated pegmatite, mylonite, and rhyolite flow tuffs, as well as in lamprophyre and felsite dikes and quartz veins, which could have originated from magmatic and/or metasomatic processes [8–14]. Rare metal granite is widely distributed in the Eastern Desert (Figure 1b). It is highly evolved granite that is distinguished by calc–alkaline, alkaline to peralkaline affinities, and A-type granite. They are widespread in orogenic belts. These rocks are subdivided into metaluminous granite (Nb, Zr, and Y rich), peraluminous granite (Ta is the most predominant one, followed by Nb, Sn, W, Be, and Li), and metasomatized granite (Nb is the most abundant, followed by Ta, Sn, Zr, Y, U, Be, and W) [15–18].

The distribution of alkali feldspar granite in the North Eastern Desert of Egypt has several favorable implications. First, crustal growth occurred, whereas the magma was derived from the mantle, then ascended through the crust, and crystallized as granite. Second, intracontinental rifting processes, which are characterized by fragmentation and splitting of continents without the involvement of plate boundaries, likely occurred. Third, the study of alkali feldspar granite can provide insights into the petrogenesis and melting processes occurring within the ANS. Fourth, heat and fluid transfers within the lithospheric layer occurred. Finally, the distribution and characteristics of alkali feldspar granite can provide insights into the tectonic setting and regional geology of the ANS. Further research and geodynamic modeling can provide deeper insights into these implications and their significance in the broader context of the ANS.

The main objective of the present work is to study the geochemical and mineralogical features of alkali feldspar granite in the ANS to understand the petrogenesis of the granite and its tectonic evolution in the studied area. This knowledge can improve our understanding of the geological and geochemical signatures of A-type granite as a good resource for rare metals mineralization in the ANS. Therefore, we proposed a geodynamic model in order to explain the origin of the Homret El Gergab alkali feldspar granite.

2. Geologic Setting

This study area is characterized by the presence of basement rocks, which are predominantly covered by Dokhan Volcanics, alkali feldspar granite, and post-granite dikes and veins, including microgranite, basaltic–andesite dikes, and quartz veins (Figure 2). The term "Dokhan Volcanics" is used to refer to a thick sequence of multicolored stratified lava flows with their pyroclastics. These rocks are hard, massive, fine-grained, and vary in color from black to greenish gray to dark gray, and from buff, pinkish-red, to reddish-brown. The pyroclastics include ash tuffs, lapilli tuffs, and agglomerates with purple ignimbrite [19–21]. They are mainly composed of basalt, andesite, rhyolite, rhyodacite, and dacite. They were dissected by quartz veins (Figure 3a).

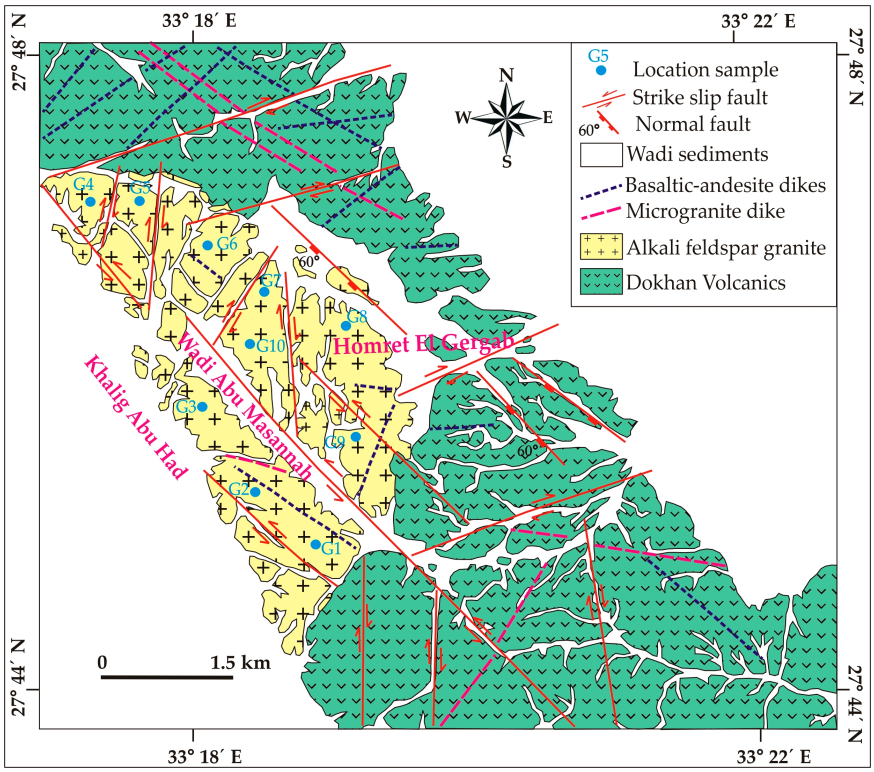

Figure 2. Geologic map of Homret El Gergab, North Eastern Desert, Egypt, modified after Abd El-Hadi [22].

Figure 3. (**a**) Quartz vein (Qz) cutting the Dokhan Volcanics (DV). (**b**) Sharp intrusive contact between the alkali feldspar granite (Gr) and Dokhan Volcanics (DV). (**c**) Exfoliation in alkali feldspar granite, (**d**,**e**). Open cut in granite for prospecting feldspars. (**f**) Distribution of alkali feldspar granite at Wadi Abu Masananah.

The Homret El Gergab granite is hard, blocky, medium- to coarse-grained, and varies in color from pink to reddish-pink and crimson. The granitic pluton occurs in the central western part of the study area and has a semicircular shape with rough terrain. It has moderately to highly elevated peaks that rise to a height of 433 m above sea level. The alkali feldspar granite intruded the Dokhan Volcanics with a markedly sharp intrusive contact (Figure 3b). Exfoliation structures are prominent features resulting from stress release, especially along the margins of the granitic pluton (Figure 3c). It is composed essentially of K-feldspar, quartz, plagioclase, and biotite. The alkali feldspar granite is cut by microgranite, basaltic, and andesite dikes and is strongly affected by faults and shear zones having E–W, NW–SE, NE–SW, and N–S trends. It shows well-defined joints and fractures. Locally, the joints and fracture planes show reddish-brown or brick-red staining, probably due to mineral solutions enriched in iron oxides. Pegmatite pockets and quartz veins are very present in the studied granite. The feldspars found in the study area are derived from alkali feldspar granite [22], specifically the Homret El Gergab pluton, which covers approximately 10 km^2 (Figure 3d–f).

3. Petrography

The alkali feldspar granite exhibits a medium- to coarse-grained hypidiomorphic texture. It is composed mainly of K-feldspar, quartz, plagioclase, and biotite. The alteration products are kaolinite, sericite, chlorite, and muscovite. Zircon, accompanied by opaque Fe-Ti oxides, are the main accessory minerals (Figure 4a–f). Perthite, a component of alkali feldspar granite, is present as well-defined crystals, in which albite lamellae are bound by/or enclosed in the perthite crystals (Figure 4a,b). The mantle is dominated by patchy and flame textures (Figure 4a). Plagioclase crystals occur as medium- to coarse-grained, subhedral to anhedral, tabular, and some show signs of erosion and are trapped within perthite. Some plagioclase crystals are displaced from their original positions and show discoloration due to the presence of iron oxides. Quartz exists as anhedral to subhedral crystals that occupy the interstitial spaces between various mineral components. In particular, it displays prominent strain patterns, including cracking and waviness, with a tendency toward undulating extinction. Biotite occurs as subhedral to anhedral crystals, and certain flakes have been partially or completely altered to chlorite and muscovite (Figure 4c,d). Zircons occur as high-relief prismatic crystals, exhibiting zonation, and are poikilitically enclosed in quartz, biotite, and opaque materials (Figure 4e,f).

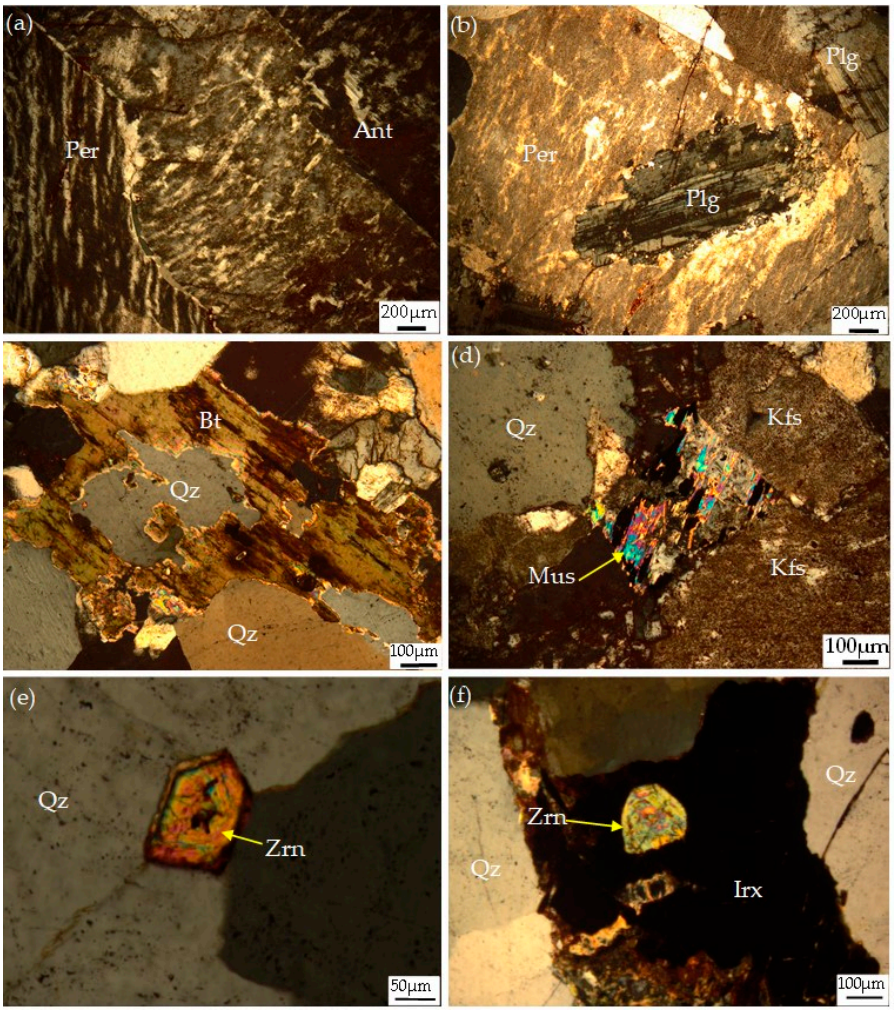

Figure 4. Photomicrographs of the studied alkali feldspar granite at Homret El Gergab, North Eastern Desert of Egypt, clarifying that (**a**) flame and patchy perthites are associated with antiperthite; (**b**) perthite encloses plagioclase; (**c**) biotite is highly altered to ferrichlorite and is associated with quartz; (**d**) fine muscovite flacks are associated with quartz; (**e**) quartz encloses euhedral zircon crystal; and (**f**) zircon is enclosed in iron oxides. Abbreviations: Per, perthite; Ant, antiperthite; Plg, plagioclase; Bt, Biotite; Qz, quartz; Mus, muscovite; Kfs, K-feldspar; Zrn, zircon; Irx, iron oxide.

4. Materials and Analytical Methods

Twenty samples were collected from the host alkali feldspar granite, and then twenty polished thin sections were obtained to identify rare metals mineralization. This work was carried out using a scanning electron microscope (FEI, Eindhoven, The Netherlands, 2006), which was mounted on the base of the analytical complex Pegasus 4000 (EDAX, Mahwah, NJ, USA). Microanalyses were performed using an electron microprobe equipped with a CAMECA SX 100 (CAMECA, Courbevoie, Île-de-France, France). The diameter of the analyzed spot on the surface of the sample was less than 1 µm at the standard temperature (15 nA beam current, 15 kV acceleration potential, 10 s counting time for peak and 5 s counting time for background; sample: iron oxide; volume: 3×10^{-19} m^3; mass: 2×10^{-12} g). The electron microprobe was equipped with five automated wavelength dispersive spectrometers (WDS) and an energy dispersive spectrometer (EDS). The WDS diffraction crystals included LiF, PET, TAP, PC0, PC1, PC2, and PC3, while the spectrometer could vary from 0.22 to 0.83 and the sin-theta had a resolution of 10^{-5}. The following natural standards were used: orthoclase for Si (Kα), albite for Al (Kα), olivine for Mg (Kα), hematite for Fe (Kα), wollastonite for Ca (Kα), and monazite for Yb (Lα). The synthetic compounds used include ThO_2, UO_2, $PbCrO_4$, ZrO_2, $CePO_4$, $NdPO_4$, $SmPO_4$, GdTiGe, $DyRu_2Ge_2$, and YPO_4, which are the corresponding standards for Th (Mα), U (Mβ), Pb (Mα), Zr (Lα), Ce (Lα), Nd (Lα), Sm (Lα), Gd (Lα), Dy (Lα), and Y (Lα), respectively.

Ten granitic samples were selected and then crushed into ten mesh particles. These particles were finely ground to a size of 200 mesh. Major oxides and trace elements were analyzed by X-ray fluorescence using an ARL 9800 f. ARL X-ray spectrometer at the Central Laboratories of St. Petersburg State University, St. Petersburg, Russia. For XRF analyses, granite powder samples were prepared with Mowiol II polyvinyl alcohol and fused with tetraborate pellets. The detection limits are 0.01% for major oxides and 1–4 ppm for trace elements.

5. Geochemistry

Whole-rock chemical compositions of the major and trace element concentrations in the Homret El Gergab alkali feldspar granite are listed in Table 1. The geochemical behavior of the major element oxides in the studied granitic samples shows that the SiO_2 content ranges from 71.2 to 74.7 wt%, the Al_2O_3 content ranges from 13.7 to 15.4 wt%, the Na_2O content ranges from 3.7 to 4.7 wt%, and the K_2O content ranges from 4.9 to 6.1 wt%. On the other hand, Fe_2O_3, CaO, MgO, and TiO_2 have low concentrations, reaching 1.8, 1.2, 0.6, and 0.3 wt%, respectively (Table 1). The Harker variation diagrams (Figure 5) illustrate a marked decrease in Al_2O_3, Fe_2O_3, and Na_2O contents with increasing SiO_2, but TiO_2, K_2O, and CaO contents show a scattered distribution of the analyzed samples.

Among the analyzed trace elements, alkali feldspar granite has a high concentration of large-ion lithophile elements (LILEs) and high-field strength elements (HFSEs), such as Rb, Zr, Ba, Y, Nb, and Th, reaching 289, 202, 180, 89, 84, and 68 ppm, respectively (Table 1). The Harker variation diagrams show a marked increase in trace elements, especially Rb, Y, Nb, Ba, and U, with increasing SiO_2, but a marked decrease in Sr, Zr, and Cr (Figure 5).

Many geochemical classifications have been proposed for igneous rocks using various geochemical parameters. The normative An-Ab-Or (anorthite-albite-orthoclase) diagram by Barker [23] shows that the analyzed samples plot in the granite field (Figure 6a). SiO_2 versus (Na_2O + K_2O) the classification diagram by Middlemost [24] (Figure 6b) reveals the studied samples plot in the alkali feldspar granite field.

Table 1. Whole-rock major element oxides (wt%), calculated CIPW norm and trace elements (ppm) of the analyzed Alkali feldspar granite, Homret El Gergab, North Eastern Desert, Egypt.

Samples	G1	G2	G3	G4	G5	G6	G7	G8	G9	G10
SiO_2	72.9	72.3	73.4	74.7	72.6	72.9	72.4	73.5	71.9	71.2
Al_2O_3	14.4	14.8	14.5	13.7	15.4	14.9	14.9	14.6	14.8	15.2
K_2O	6.10	5.90	4.90	5.60	5.10	5.20	5.30	5.10	5.70	5.00
Na_2O	3.66	4.17	4.12	4.04	4.41	4.4	4.52	4.32	4.23	4.66
Fe_2O_3	1.35	1.78	1.44	1.21	1.25	1.33	1.39	1.10	1.52	1.61
CaO	0.89	0.47	0.91	0.52	0.78	0.71	0.8	0.76	1.05	1.16
MgO	0.29	0.20	0.40	0.07	0.19	0.23	0.26	0.16	0.14	0.58
TiO_2	0.24	0.22	0.15	0.12	0.12	0.15	0.14	0.15	0.17	0.29
MnO	0.04	0.03	0.02	0.02	0.01	0.02	0.02	0.02	0.03	0.06
P_2O_5	0.01	0.03	0.02	0.03	0.02	0.01	0.05	0.01	0.04	0.03
L.O.I.	0.20	0.10	0.20	0.10	0.10	0.20	0.20	0.30	0.20	0.10
Total	100	99.9	100	99.9	99.9	100	100	100	99.7	99.9
Q	26.0	24.3	28.2	28.6	25.5	25.6	23.9	27.0	23.2	21.7
C	0.20	0.80	0.80	0.10	1.30	0.80	0.40	0.60	0.00	0.10
Or	36.0	34.9	29.0	33.1	30.1	30.7	31.3	30.1	33.7	29.5
Ab	31.0	35.3	34.9	34.2	37.3	37.2	38.2	36.6	35.8	39.4
An	4.40	2.10	4.40	2.40	3.70	3.50	3.60	3.70	4.60	5.60
Di	0.00	0.00	0.00	0.00	0.00	0.00	0.00	0.00	0.00	0.00
Hy	0.70	0.50	1.00	0.20	0.50	0.60	0.60	0.40	0.30	1.40
Mt	0.00	0.00	0.00	0.10	0.00	0.00	0.00	0.00	0.00	0.00
Il	0.10	0.10	0.00	0.00	0.00	0.00	0.00	0.00	0.10	0.10
Hm	1.40	1.80	1.40	1.20	1.30	1.30	1.40	1.10	1.50	1.60
Tn	0.00	0.00	0.00	0.00	0.00	0.00	0.00	0.00	0.30	0.00
Ru	0.20	0.20	0.10	0.00	0.10	0.10	0.10	0.10	0.00	0.20
Ap	0.00	0.10	0.00	0.10	0.00	0.00	0.10	0.00	0.10	0.10
Trace elements (ppm)										
V	48.0	46.0	36.0	26.0	26.0	38.0	34.0	31.0	29.0	63.0
Cr	44.0	23.0	15.0	11.0	17.0	19.0	18.0	8.00	19.0	37.0
Co	26.0	15.0	10.0	19.0	9.80	66.0	12.0	26.0	7.00	39.0
Cu	3.00	10.0	18.0	8.00	11.0	75.0	6.00	28.0	16.0	7.00
Zn	18.0	28.0	21.0	14.0	32.0	11.0	14.0	11.0	18.0	18.0
As	5.00	2.00	7.00	5.00	4.00	9.00	6.00	2.00	6.00	5.00
Zr	185	202	127	112	138	142	145	142	196	139
Mo	13.0	9.00	5.00	22.0	9.00	8.00	6.00	10.0	8.00	6.00
Cd	21.0	14.0	5.00	4.00	12.0	23.0	18.0	23.0	31.0	12.0
Sn	5.00	21.0	8.00	4.00	3.00	7.60	19.0	5.90	5.00	4.70
Pb	15.0	14.0	14.0	9.00	12.0	9.00	15.0	12.0	11.0	11.0
U	25.0	23.0	27.0	21.0	26.0	29.0	27.0	23.0	25.0	22.0
Th	34.0	39.0	42.0	44.0	33.0	45.0	43.0	36.0	46.0	45.0
Rb	224	202	269	281	289	252	232	245	277	210
Sr	37.0	41.0	27.0	16.0	16.0	35.0	27.0	21.0	26.0	39.0
Ni	5.30	4.60	3.00	6.50	6.00	8.00	4.00	9.00	5.00	3.00
Nb	74.0	66.0	84.0	59.0	74.0	66.0	71.0	80.0	52.0	59.0
Ga	16.0	22.0	26.0	15.0	8.00	19.0	23.0	9.50	28.0	22.0
Y	67.0	54.0	89.0	69.0	73.0	82.0	44.0	73.0	71.0	60.0
Hf	2.30	3.10	0.90	2.10	0.80	0.70	2.10	3.50	3.90	4.40
Ba	115	120	143	180	98.0	150	144	167	84.0	139
TZr °C	795	805	767	753	775	775	773	775	794	766
Th/U	0.74	0.59	0.64	0.48	0.79	0.64	0.63	0.64	0.54	0.49
Rb/Sr	6.05	4.93	9.96	17.56	18.06	7.20	8.59	11.67	10.65	5.38

TZr °C (zircon saturation temperature).

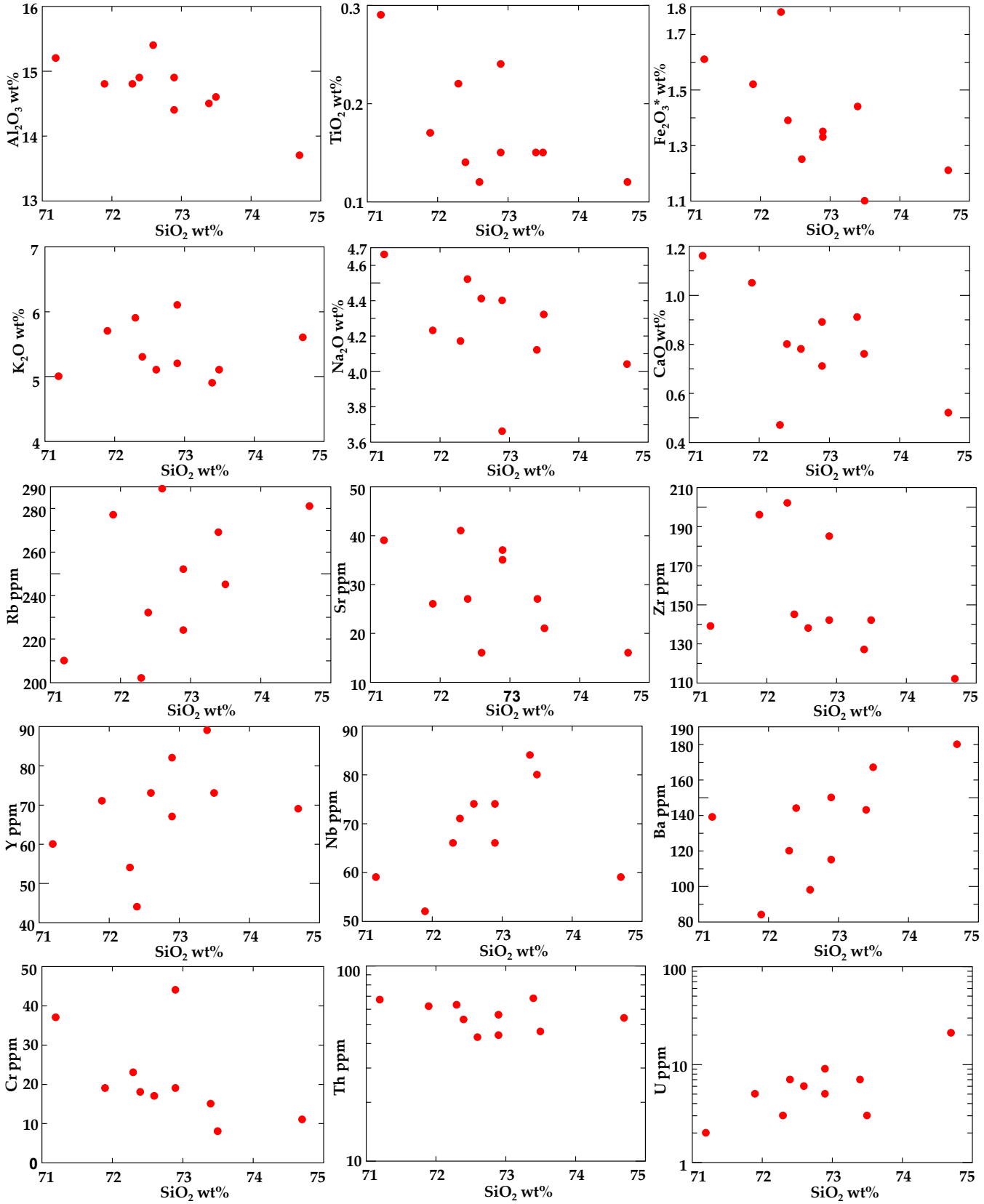

Figure 5. Harker variation diagrams illustrate the distributions of major oxides and trace elements in relation to silica in the studied granite.

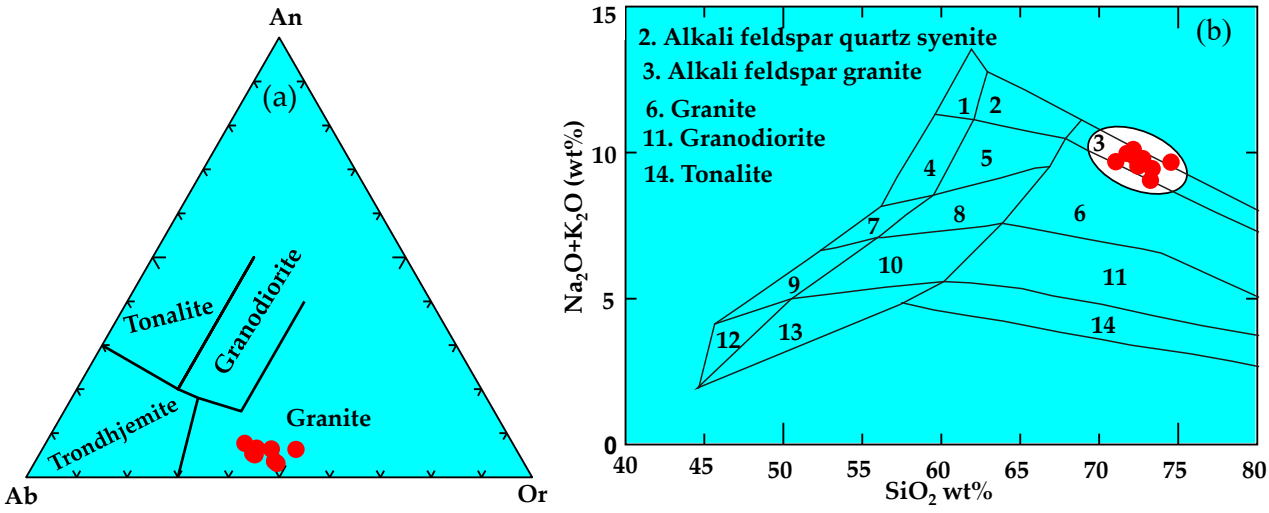

Figure 6. Geochemical discrimination diagrams present the nomenclature of the studied granite. (**a**) Ternary An–Ab–Or normative diagram by Barker [23]. (**b**) Binary diagram shows the total alkalis versus silica, according to Middlemost [24].

The concentrations of multiple elements were normalized to those of the primitive mantle values of Sun and McDonough [25], which could provide a general indication of the source and tectonic affinities of the studied granite (Figure 7). The analyzed alkali feldspar granite is strongly enriched in Rb, as a large ion lithophile element (LILE), when compared with high-field strength elements (HFSE; Nb, Zr, Y), but depleted in Ba, Sr, P, and Ti elements with marked troughs. The negative anomalies in P and Sr elements could mark fractionation of apatite and feldspars at the source or during differentiation. The differences in trace element contents in the studied granite may be a clue to the different degrees of partial melting or fractional crystallization. Ti depletion could be related to the fractionation of biotite or titanomagnetite.

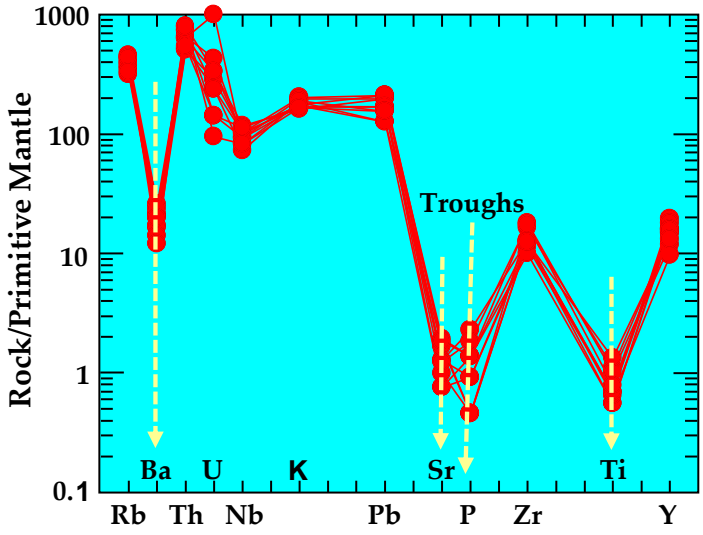

Figure 7. Normalized multi-element pattern according to Sun and McDonough [25] of the studied granite.

Figure 8 illustrates the geochemical behavior of U and Th in the studied alkali feldspar granite. The histograms show that Th ranges from 33 to 46 ppm and U ranges from 21 to 29 ppm (Table 1). The Th/U ratio of the analyzed alkali feldspar granite ranges from 0.48 to 3.8, which is lower than the upper crust value of 3.8 [26]. Thorium is an immobile element; therefore, this ratio mainly depends on the content of uranium, which is a mobile

element. The analyzed granite samples have a lower Th/U ratio, which could be related to U enrichment.

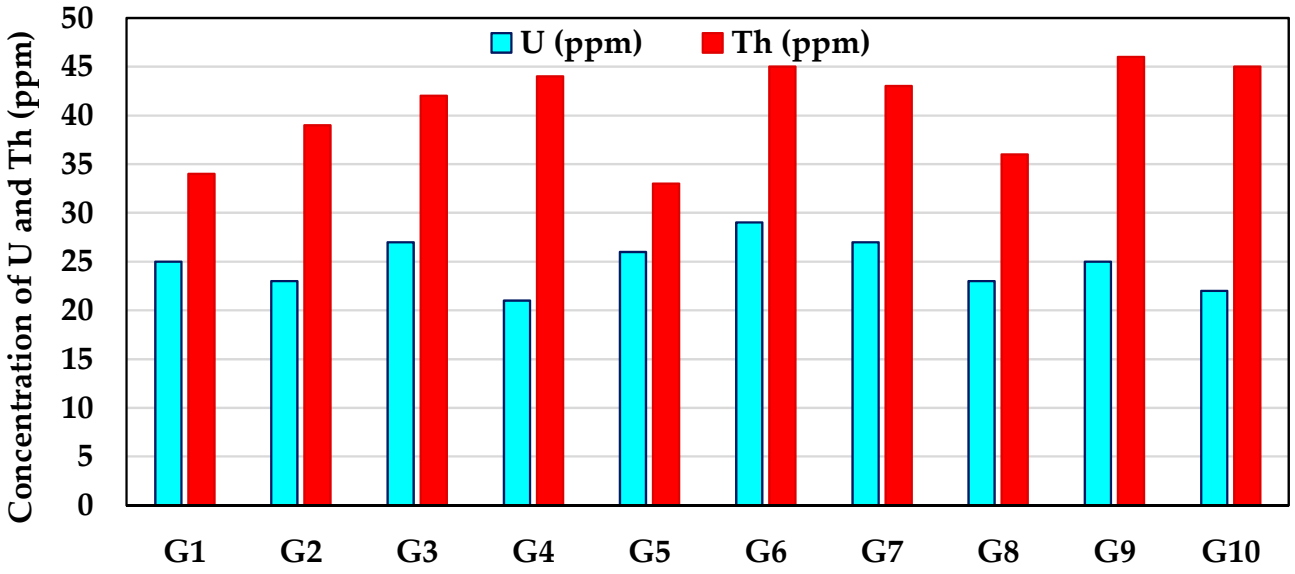

Figure 8. Histograms showing the concentrations of U and Th in the studied granitic samples from Homret El Gergab, North Eastern Desert, Egypt.

6. Mineral Chemistry

6.1. Radioactive Minerals

6.1.1. Uranothorite

It usually occurs as tiny individual crystals (<10 µm) that are anhedral and are often associated with monazite (Figure 9a). The EPMA data show that uranothorite is composed essentially of ThO_2, ranging from 53.74 to 54.24 wt%; SiO_2, from 15.66 to 16.27 wt%; and UO_2, from 13.25 to 14.21 wt%. LREEs, including La, Ce, Nd, and Sm, have been reported, and $\Sigma LREE_2O_3$ (La–Sm) ranges from 3.71 to 4.45 wt%. Fe_2O_3, CaO, and P_2O_5 are well documented in small amounts (Table 2).

Table 2. Representative EMPA of uranothorite (oxides in wt%) from Alkali feldspar granite at Homret El Gergab, North Eastern Desert, Egypt.

ThO_2	53.85	53.79	54.24	53.74
SiO_2	15.98	16.01	16.27	15.66
UO_2	13.25	14.21	14.12	13.92
La_2O_3	0.25	0.31	0.34	0.27
Ce_2O_3	1.78	1.86	1.91	1.81
Nd_2O_3	1.24	1.61	1.58	1.31
Sm_2O_3	0.44	0.67	0.53	0.46
CaO	1.53	1.78	1.12	1.45
P_2O_5	0.84	0.68	0.61	0.43
Fe_2O_3	1.49	1.57	1.56	1.61
Total	90.65	92.49	92.28	90.66
$\Sigma LREE_2O_3$	3.71	4.45	4.36	3.85
		Calculated formulae (apfu)		
Th	0.71	0.70	0.70	0.72
Si	0.92	0.91	0.93	0.92
U	0.17	0.18	0.18	0.18
La	0.01	0.01	0.01	0.01
Ce	0.04	0.04	0.04	0.04
Nd	0.03	0.03	0.03	0.03
Sm	0.01	0.01	0.01	0.01
Ca	0.09	0.11	0.07	0.09
P	0.04	0.03	0.03	0.02
Fe	0.06	0.07	0.07	0.07
Sum	2.07	2.09	2.07	2.08

Calculated chemical formula based on 4 oxygen (apfu) for uranothorite.

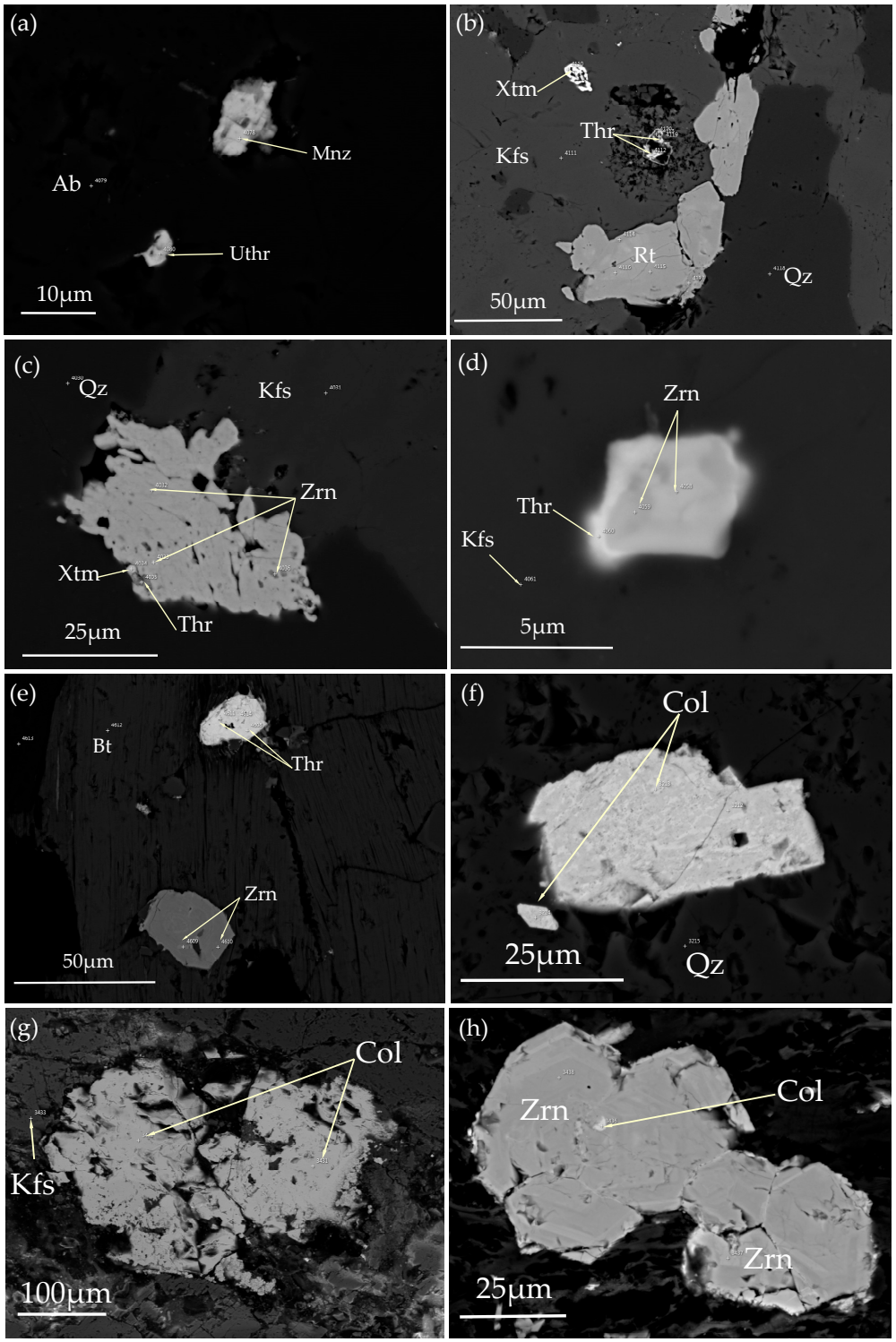

Figure 9. Back-scattered images (BSE) of radioactive minerals associated with other accessory minerals from alkali feldspar granite, Homret El Gergab, North Eastern Desert, Egypt. (**a**) Fine-grained uranothorite is associated with monazite and is enclosed in feldspar. (**b**) Fine-grained xenotime and thorite are associated with rutile. (**c**) Fine-grained xenotime and thorite occur along the rims of zircon. (**d**) Thin films of thorite occur along the periphery of zircon. (**e**) Thorite and zircon are enclosed in biotite. (**f**) Columbite crystals are enclosed in quartz. (**g**) Highly deformed columbite crystals are enclosed in K-feldspar. (**h**) Large zircon crystals enclose microinclusions of columbite. Abbreviations: uthr, uranothorite; thr, thorite; Zrn, zircon; Mnz, monazite; Xtm, xenotime; Col, columbite; Rt, rutile; Qz, quartz; Ab, Albite; Kfs, K-feldspar; Bt, Biotite.

6.1.2. Thorite

Th-silicate minerals are abundant and predominant in the investigated alkali feldspar granite in the study area. These grains occur as fine individual crystals and/or adjacent thin films (bright colors) along the peripheries of zircon crystals (Figure 9b–e). It consists of anhedral crystals that are <10 µm in length, is accompanied by zircon, xenotime, and rutile, and is always enclosed in feldspar and quartz crystals. It occurs as bright microinclusions and/or adjacent to zircon crystals (Figure 9b–e). The analyzed EPMA data (Table 3) show that thorite is essentially composed of ThO_2 ranging from 51.27 to 52.73 wt% and SiO_2 ranging from 16.17 to 18.35 wt%. UO_2 is well represented in thorite, with higher concentrations reaching up to 7.1 wt% (Table 3). Y_2O_3-bearing thorite is present and ranges from 2 to 3.2 wt%. The higher concentrations of ΣREE_2O_3 (La–Er) range from 9.35 to 14.1 wt%. Ce_2O_3 is the most abundant REE and reaches up to 4.3 wt% of the other elements. Moreover, CaO, P_2O_5, Fe_2O_3, and Al_2O_3 are well represented in the analyzed thorite at low concentrations (Table 3).

Table 3. Representative EMPA of thorite (oxides in wt%) from alkali feldspar granite at Homret El Gergab, North Eastern Desert, Egypt.

ThO_2	51.35	51.27	52.73	52.17	51.33	52.22
SiO_2	18.35	17.27	17.73	16.17	17.33	16.22
UO_2	2.94	5.66	3.16	7.1	4.73	2.93
La_2O_3	0.54	1.31	1.23	1.24	1.29	1.76
Ce_2O_3	1.98	1.32	1.51	1.92	0.96	4.30
Nd_2O_3	1.29	1.17	1.33	1.66	1.45	2.30
Sm_2O_3	1.32	1.29	1.37	1.40	1.46	1.48
Gd_2O_3	1.74	1.61	1.81	1.87	1.94	1.97
Dy_2O_3	2.10	2.15	1.99	2.00	1.94	1.97
Er_2O_3	0.54	1.19	0.73	0.66	0.31	0.32
Y_2O_3	3.20	2.51	1.84	2.59	2.89	2.01
P_2O_5	1.73	1.28	1.08	1.65	1.58	2.06
CaO	0.77	0.92	0.78	1.04	1.04	0.74
Fe_2O_3	1.69	1.76	2.02	1.39	1.34	1.22
Al_2O_3	0.91	0.87	0.76	0.69	0.85	0.94
Total	90.45	91.58	90.07	93.55	90.44	92.44
ΣREE_2O_3	9.51	10.04	9.97	10.75	9.35	14.1
			Calculated formulae (apfu)			
Th	0.61	0.62	0.65	0.64	0.63	0.64
Si	0.96	0.92	0.96	0.87	0.93	0.87
U	0.03	0.07	0.04	0.09	0.06	0.03
La	0.01	0.03	0.02	0.02	0.03	0.03
Ce	0.04	0.03	0.03	0.04	0.02	0.08
Nd	0.02	0.02	0.03	0.03	0.03	0.04
Sm	0.02	0.02	0.03	0.03	0.03	0.03
Gd	0.03	0.03	0.03	0.03	0.03	0.03
Dy	0.04	0.04	0.03	0.03	0.03	0.03
Er	0.01	0.02	0.01	0.01	0.01	0.01
Y	0.09	0.07	0.05	0.07	0.08	0.06
P	0.08	0.06	0.05	0.08	0.07	0.09
Ca	0.04	0.05	0.05	0.06	0.06	0.04
Fe	0.07	0.07	0.08	0.06	0.05	0.05
Al	0.06	0.05	0.05	0.04	0.05	0.06
Sum	2.10	2.11	2.10	2.10	2.10	2.11

Calculated chemical formula based on 4 oxygen (apfu) for thorite.

6.2. Columbite

Columbite occurs as tabular, subhedral to anhedral crystals that are massive and vary in size from 100 to 400 µm (Figure 9f,g). They are commonly enclosed in K-feldspar, quartz, and plagioclase crystals, whereas others are commonly dispersed as microinclusions in zircon crystals (Figure 9f,g). The EPMA data show that columbite is composed of Nb_2O_5 at concentrations ranging from 66.49 to 74.7 wt% and Fe_2O_3 at concentrations ranging from 17.27 to 26.42 wt%, whereas MnO has a lower concentration ranging from 0.5 to 5.78 wt%. TiO_2, Ta_2O_5, and Y_2O_3 have low concentrations (Table 4). The radioactive elements uranium and thorium have low contents in the analyzed columbite, reaching 3.09 wt% for UO_2 and 1.53 wt% for ThO_2.

Table 4. Representative EMPA of columbite (oxides in wt%) from alkali feldspar granite at Homret El Gergab, North Eastern Desert, Egypt.

Nb_2O_5	70	69.21	70.09	74.7	70.95	72.8	66.49	67.76	70.84
Ta_2O_5	0.77	n.d.	n.d.	n.d.	3.44	3.44	3.03	n.d.	2.55
TiO_2	2.67	0.80	1.73	2.82	1.78	0.63	2.84	1.33	1.51
Fe_2O_3	23.56	23.39	25.35	20.93	19.44	17.27	23.91	26.42	22.6
MnO	1.58	0.57	1.01	1.46	1.25	5.78	n.d.	0.68	0.50
Y_2O_3	n.d.	2.92	n.d.	n.d.	n.d.	n.d.	2.46	1.74	1.93
ThO_2	0.44	1.53	0.64	n.d.	n.d.	n.d.	1.40	1.11	n.d.
UO_2	1.00	1.53	1.24	n.d.	3.09	n.d.	n.d.	0.98	n.d.
Total	100	100	100	100	100	100	100	100	100
				Calculated formulae (apfu)					
Nb	1.69	1.71	1.70	1.78	1.76	1.80	1.62	1.65	1.72
Ta	0.01				0.05	0.05	0.04		0.04
Ti	0.11	0.03	0.07	0.11	0.07	0.03	0.12	0.05	0.06
Fe	0.95	0.96	1.02	0.83	0.80	0.71	0.97	1.07	0.91
Mn	0.07	0.03	0.05	0.07	0.06	0.27		0.03	0.02
Y		0.08					0.07	0.05	0.06
Th	0.01	0.02	0.01				0.02	0.01	
U	0.01	0.02	0.01		0.04			0.01	
∑cation	2.85	2.85	2.85	2.79	2.78	2.85	2.84	2.88	2.81
Ta/(Ta + Nb)	0.01				0.03	0.03	0.02		0.02
Mn/(Mn + Fe)	0.07	0.03	0.05	0.08	0.07	0.28		0.03	0.02

The chemical formula was calculated for columbite based on 6 oxygen atoms (apfu). n.d. not determined.

6.3. Zircon

Zircon crystals occur in various shapes, ranging from prismatic to subhedral or anhedral crystals (Figures 9 and 10). Zircon inclusions can range in size from being as small as microinclusions in K-feldspar crystals to larger single crystals that can reach up to 50 µm in size. Some of these zircon crystals appear to be heavily corroded and contain dark patches. In addition, bright xenotime and thorite can be found at the edges of the zircon crystals. The EPMA data show that the zircon crystals are composed of ZrO_2, which ranges from 58.05 and 61.1 wt%, and SiO_2, which ranges from 29.1 and 32.67 wt%. Other elements present include HfO_2, which ranges from 1.43 to 3.61 wt%, and Sc_2O_3, which from 0.26 to 0.64 wt%. Al_2O_3, CaO, MnO, and Fe_2O_3 are recorded in low concentrations (Table 5). The two radioactive elements reached 4.38 wt% for UO_2 and 3.89 wt% for ThO_2.

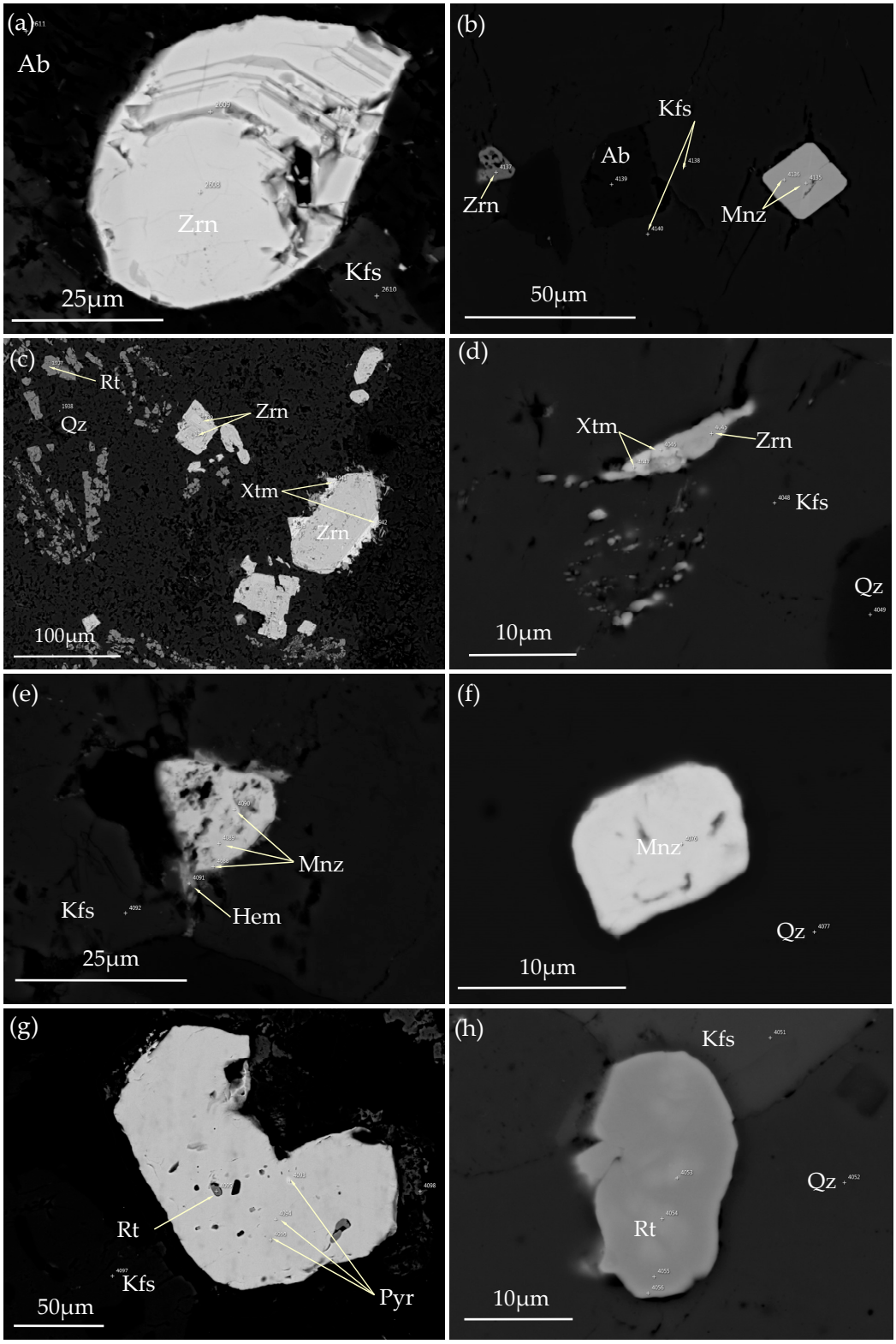

Figure 10. Back-scattered images (BSE) of Zr and REE minerals associated with other accessories from alkali feldspar granite, Homret El Gergab, North Eastern Desert, Egypt. (**a**) Zoned zircon crystals are enclosed in feldspar. (**b**) Fine-grained monazite and zircon are enclosed in feldspar. (**c**) Xenotime is overgrown along the rims of zircon. (**d**) Fine-grained xenotime is adjacent to zircon. (**e**) Hematite is along the periphery of monazite. (**f**) Quartz encloses monazite. (**g**) Pyrite encloses rutile. (**h**) Quartz encloses rutile. Abbreviations: Zrn, zircon; Mnz, monazite; Xtm, xenotime; Rt, rutile; Hem, hematite; Qz, quartz; Ab, Albite; Kfs, K-feldspar.

Table 5. Representative EMPA of zircon (oxides in wt%) from alkali feldspar granite at Homret El Gergab, North Eastern Desert, Egypt.

SiO_2	30.09	31.2	31.04	31.75	31.12	30.11	30.07	32.16	32.13	29.56	29.97	29.1	32.67	30.5	31.14
ZrO_2	58.25	60.33	59.28	59.59	61.1	58.25	58.24	59.78	58.55	58.05	58.25	58.15	59.36	61.03	59.33
HfO_2	2.84	3.61	3.57	3.25	3.53	3.02	3.31	2.91	1.90	1.43	1.51	1.52	1.76	3.60	3.57
Sc_2O_3	0.38	0.31	0.41	0.26	0.28	0.34	0.38	0.35	0.29	0.31	0.38	0.64	0.39	0.42	0.41
CaO	0.84	0.76	1.12	1.05	0.62	0.92	0.69	0.81	0.97	1.01	0.85	1.15	0.81	0.76	1.12
Fe_2O_3	1.53	0.7	0.79	1.06	0.56	1.02	1.09	0.97	0.89	1.04	2.27	1.46	1.03	0.70	0.79
Al_2O_3	0.59	0.49	0.79	0.53	0.36	0.66	0.47	0.59	0.64	0.42	0.54	0.58	0.59	0.49	0.79
MnO	0.5	0.61	0.56	0.6	0.44	0.39	0.45	0.45	0.41	0.53	0.38	0.57	0.64	0.61	0.56
ThO_2	3.89	1.32	1.15	0.97	1.12	3.29	3.35	0.91	0.85	3.31	3.41	3.57	1.25	1.21	1.05
UO_2	1.17	0.67	1.33	1.00	0.93	2.00	1.95	1.10	3.46	4.38	2.44	3.27	1.59	0.67	1.33
Total	100	100	100	100	100	100	100	100	100	100	100	100	100	100	100
Calculated formulae (apfu)															
Si	0.96	0.98	0.98	0.99	0.98	0.96	0.96	1.00	1.00	0.96	0.98	0.94	1.01	0.96	0.98
Zr	0.91	0.92	0.91	0.91	0.94	0.91	0.91	0.91	0.89	0.92	0.90	0.92	0.89	0.94	0.91
Hf	0.03	0.03	0.03	0.03	0.03	0.03	0.03	0.03	0.02	0.01	0.01	0.01	0.02	0.03	0.03
Sc	0.01	0.01	0.01	0.01	0.01	0.01	0.01	0.01	0.01	0.01	0.01	0.01	0.01	0.01	0.01
Ca	0.03	0.03	0.04	0.04	0.02	0.03	0.02	0.03	0.03	0.04	0.00	0.04	0.03	0.03	0.04
Fe	0.04	0.02	0.02	0.02	0.01	0.02	0.03	0.02	0.02	0.03	0.05	0.04	0.02	0.02	0.02
Al	0.02	0.02	0.03	0.02	0.01	0.02	0.02	0.02	0.02	0.02	0.02	0.02	0.02	0.02	0.03
Mn	0.01	0.02	0.01	0.02	0.01	0.01	0.01	0.01	0.01	0.01	0.01	0.02	0.02	0.02	0.01
Th	0.03	0.01	0.01	0.01	0.01	0.02	0.02	0.01	0.01	0.02	0.02	0.03	0.01	0.01	0.01
U	0.01	0.00	0.01	0.01	0.01	0.01	0.01	0.01	0.02	0.03	0.02	0.02	0.01	0.00	0.01
Sum	2.04	2.03	2.04	2.04	2.03	2.04	2.03	2.03	2.04	2.04	2.03	2.05	2.04	2.03	2.04

Calculated chemical formula based on 4 oxygen (apfu) for zircon.

6.4. REE Phosphates

Phosphate minerals are recorded in alkali feldspar granite. They include monazite and xenotime, and they are considered good sources of LREEs and HREEs, respectively, as well as Y (Section 6.4.2).

6.4.1. Monazite-Ce

Monazite-Ce is a common LREE phosphate mineral that occurs as euhedral to anhedral and fine- to medium-grained (Figure 10b,e,f). From the analyzed EPMA data, monazite chemistry reveals that P_2O_5 ranges from 27.37 to 29.84 wt%, with a marked enrichment in LREEs, while the $\sum REE_2O_3$ (La_2O_3–Gd_2O_3) concentration ranges from 59.15 wt% to 65.75 wt% (Table 6). Ce_2O_3 is the most abundant LREE in the analyzed monazite grains, reaching 30.51 wt%, followed by Nd_2O_3, reaching 16.76 wt%, La_2O_3, reaching 12.93 wt%, and others (Table 6). Gd_2O_3 is the only recorded HREE in the analyzed monazite and ranges from 1.29 to 3.19 wt%. Enrichment in ThO_2 was clearly observed in the monazite grains, ranging from 4.85 to 10.41 wt% (Table 6). CaO was recorded in smaller amounts, ranging from 0.69 to 3.37 wt%. The average empirical formula for monazite is $(Ce_{0.42}Nd_{0.19}La_{0.15}Pr_{0.05}Sm_{0.06}Gd_{0.03}Th_{0.07})(P_{0.98})O_4$. Monazite has shown a predominance of Ce (0.42 apfu) over other REEs corresponding to monazite-Ce. The geochemical compositions of the monazite crystals are remarkably similar, and the chemical reactions are carried out by the following substitutions:

$$Th^{4+} + Si^{4+} \leftrightarrow REE^{3+} + P^{5+}$$

$$Th^{4+} + Ca^{2+} \leftrightarrow 2REE^{3+}$$

As recorded by Watt [27], Abd El Ghaffar [28], and Abdel Gawad [29].

Table 6. Representative EMPA of monazite (oxides in wt%) from alkali feldspar granite at Homret El Gergab, North Eastern Desert, Egypt.

P_2O_5	27.45	27.37	29.69	29.84	29.04	28.5	28.53	29.17	29.48	28.45	28.2	28.88	27.42
CaO	1.06	1.16	1.19	1.15	3.37	1.11	0.70	0.69	2.69	0.71	1.19	1.19	0.84
La_2O_3	8.03	12.29	11.9	11.99	12.93	9.69	10.71	8.39	10.92	8.78	7.00	10.17	8.89
Ce_2O_3	28.31	29.48	28.52	29.95	29.61	28.46	30.18	28.05	30.51	28.38	28.42	27.35	28.11
Pr_2O_3	3.92	4.22	3.75	2.66	4.07	4.04	3.97	2.72	2.98	3.23	3.71	3.73	3.87
Nd_2O_3	14.13	11.57	10.25	9.70	11.13	15.2	13.44	15.92	11.85	15.27	13.41	15.98	16.76
Sm_2O_3	4.26	4.24	3.31	3.64	3.06	4.58	3.79	4.96	2.74	4.59	4.95	3.99	5.04
Gd_2O_3	2.46	1.29	1.42	1.52	1.75	2.26	2.46	2.59	1.83	3.19	3.01	1.96	3.08
ThO_2	10.41	8.46	9.92	9.14	4.85	6.15	6.19	7.60	6.65	7.39	10.18	6.85	6.00
Total	100	100	99.95	99.59	99.81	100	100	100	99.65	100	100	100	100
ΣREE_2O_3	61.11	63.09	59.15	59.46	62.55	64.23	64.55	62.63	60.83	63.44	60.5	63.18	65.75
Calculated formulae (apfu)													
P	0.96	0.95	1.00	1.00	0.97	0.97	0.98	0.99	0.98	0.98	0.97	0.98	0.95
Ca	0.05	0.05	0.05	0.05	0.14	0.05	0.03	0.03	0.11	0.03	0.05	0.05	0.04
La	0.12	0.19	0.17	0.18	0.19	0.14	0.16	0.12	0.16	0.13	0.11	0.15	0.13
Ce	0.43	0.44	0.41	0.43	0.43	0.42	0.45	0.41	0.44	0.42	0.42	0.4	0.42
Pr	0.06	0.06	0.05	0.04	0.06	0.06	0.06	0.04	0.04	0.05	0.05	0.05	0.06
Nd	0.21	0.17	0.15	0.14	0.16	0.22	0.19	0.23	0.17	0.22	0.19	0.23	0.25
Sm	0.06	0.06	0.05	0.05	0.04	0.06	0.05	0.07	0.04	0.06	0.07	0.06	0.07
Gd	0.03	0.02	0.02	0.02	0.02	0.03	0.03	0.03	0.02	0.04	0.04	0.03	0.04
Th	0.10	0.08	0.09	0.08	0.04	0.06	0.06	0.07	0.06	0.07	0.09	0.06	0.06
Sum	2.01	2.02	1.99	1.99	2.05	2.01	2.01	1.99	2.03	2.00	2.01	2.01	2.02

Calculated chemical formula based on 4 oxygen (apfu) for monazite; ΣREE_2O_3 (La_2O_3–Gd_2O_3).

6.4.2. Xenotime

Xenotime is anhedral to subhedral, fine-grained, and often enclosed in K-feldspar crystals. It is predominantly accompanied by zircon, thorite, and rutile (Figures 9b,c and 10c,d). EPMA data show that the analyzed xenotime is a good source of HREEs (Table 7). The chemical data show that P_2O_5 ranges from 30.23 to 32.15 wt%, Y_2O_3 ranges from 45.22 to 48.64 wt%, and $\sum HREE_2O_3$ (Gd_2O_3–Lu_2O_3) ranges from 15.45 to 17.9 wt%. In addition, xenotime has higher concentrations of Dy_2O_3, Er_2O_3, and Yb_2O_3 (Table 7). It has higher concentrations of radioactive elements, especially ThO_2, which ranges from 1.55 to 5.44 wt%, whereas UO_2 reaches up to 1.51 wt%. CaO and Fe_2O_3 were presented as minor constituents.

Table 7. Representative EMPA of xenotime (oxides in wt%) from studied alkali feldspar granite at Homret El Gergab, North Eastern Desert, Egypt.

Y_2O_3	48.64	45.36	46.4	45.22	46.3
Gd_2O_3	2.69	2.74	2.26	2.49	2.39
Dy_2O_3	4.50	4.40	3.09	4.11	4.21
Ho_2O_3	1.15	0.77	0.78	1.09	0.66
Er_2O_3	3.02	2.79	2.98	3.46	3.46
Tm_2O_3	1.61	1.54	1.51	1.67	1.62
Yb_2O_3	2.16	2.13	3.11	3.33	3.33
Lu_2O_3	1.34	1.36	1.72	1.75	1.69
P_2O_5	30.35	30.23	31.33	32.15	31.65
CaO	1.33	1.36	1.41	1.38	1.36
Fe_2O_3	0.81	0.75	0.83	0.79	0.80
ThO_2	1.55	5.44	3.07	1.64	1.64
UO_2	0.93	1.13	1.51	0.94	0.94
Total	100	100	100	100	100
$\Sigma HREE_2O_3$	16.47	15.73	15.45	17.90	17.36
		Calculated formulae (apfu)			
Y	0.91	0.85	0.86	0.83	0.85

Table 7. *Cont.*

Gd	0.03	0.03	0.03	0.03	0.03
Dy	0.05	0.05	0.03	0.05	0.05
Ho	0.01	0.01	0.01	0.01	0.01
Er	0.03	0.03	0.03	0.04	0.04
Tm	0.02	0.02	0.02	0.02	0.02
Yb	0.02	0.02	0.03	0.03	0.04
Lu	0.01	0.01	0.02	0.02	0.02
P	0.90	0.91	0.92	0.94	0.93
Ca	0.05	0.05	0.05	0.05	0.05
Fe	0.02	0.02	0.02	0.02	0.02
Th	0.01	0.04	0.02	0.01	0.01
U	0.01	0.01	0.01	0.01	0.01
Sum	2.08	2.06	2.06	2.05	2.06

Calculated chemical formula based on 4 oxygen (apfu) for xenotime; ΣREE_2O_3 (Gd_2O_3–Lu_2O_3).

6.5. Other Accessory Minerals

Pyrite occurs as coarse-grained, equant plates, euhedral to subhedral, and encloses rutile microinclusions (gray to black colors) (Figure 10g). It is enclosed in feldspar. The analyzed EPMA data show that pyrite is essentially composed of Fe ranging from 46.25 to 47 wt% and S ranging from 53 to 53.75 wt%.

Rutile is the most abundant accessory mineral. It occurs as anhedral to subhedral, fine- to medium-grained microinclusions in ilmenite and is associated with thorite, zircon, monazite, xenotime, and ilmenite (Figures 9b and 10c,h). The EMPA data indicate that rutile is composed of TiO_2 in the range of 98.12 to 99.9 wt%, Fe_2O_3 from 0.61 to 3.66 wt%, and Nb_2O_5 from 3 to 4.62 wt%.

Ilmenite occurs along the periphery of rutile and is enclosed in feldspars. It is associated with monazite and zircon. The EMPA data show that ilmenite is mainly composed of TiO_2, ranging from 46.25 to 47.66 wt%; Fe_2O_3, from 51.01 to 53.2 wt%; and MnO, from 0.45 to 0.87 wt%.

7. Discussion

7.1. Magma Type and Tectonic Setting Signature

Several discrimination diagrams have been proposed and used to elucidate the magma types of igneous rocks. Maniar and Piccoli [30] used $(Al_2O_3)/(Na_2O + K_2O + CaO)$ versus $(Al_2O_3)/(Na_2O + K_2O)$ to distinguish between peraluminous, metaluminous, and peralkaline rocks. Figure 11a shows the granite under study concentrated in the peraluminous field. For the subalkaline rocks, Rickwood [31] used the K_2O versus SiO_2 discrimination diagram (Figure 11b) to differentiate between the shoshonite series, high-K calc–alkaline series, medium-K calc–alkaline series, and low-K tholeiites. The studied granite samples plot in the calc–alkaline series high-K field.

Several tectonic setting discrimination variation diagrams have been proposed for granites. Rb versus (Y + Nb) and Nb versus Y discrimination diagrams by Pearce et al. [32] are used to distinguish between volcanic arc granite (VAG), syn-collision granite (Syn-COLG), ocean ridge granite (ORG), and within-plate granite (WPG). The figures show that the study samples are plotted in the within-plate regime field (Figure 12a,b). By utilizing various diagrams, Whalen et al. [33] distinguished between two groups of granites with different tectonic settings. Granites are subdivided into (1) those generated during the evolution of fold belts (orogenic), such as I-, S-, and M-types [34–36], and (2) those associated with uplift and major strike-slip faulting (anorogenic), such as A-types [37–39]. In Figure 12c,d, the plotting of 10,000*Ga/Al versus K_2O/MgO and Nb indicates that the studied alkali feldspar granite is plotted in A-type granite.

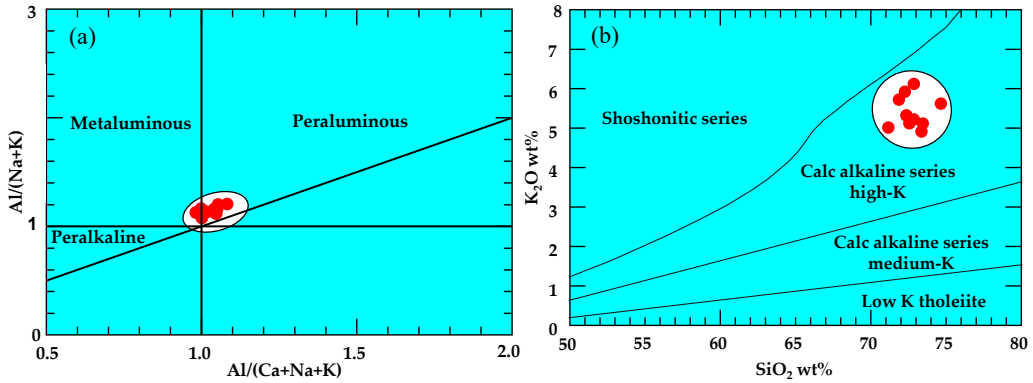

Figure 11. Magma-type discrimination diagrams of the studied granite. (**a**) Binary molar $Al_2O_3/(Na_2O + K_2O)$ versus $Al_2O_3/(CaO + Na_2O + K_2O)$ diagram of Maniar and Piccoli [30]. (**b**) Binary K_2O versus SiO_2 diagram of Rickwood [31].

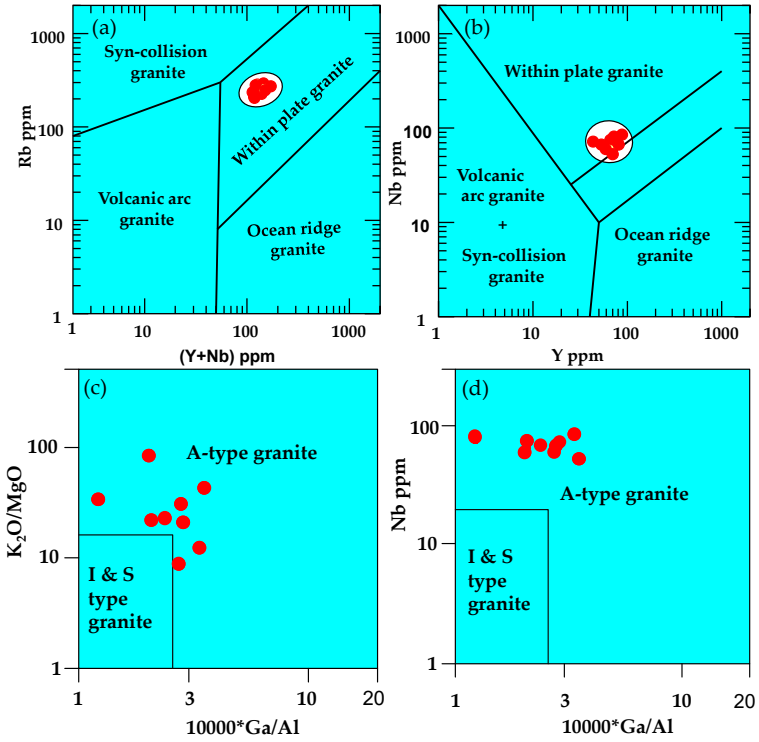

Figure 12. Tectonic setting discrimination diagrams of the studied granite. (**a**) Binary Rb versus (Y + Nb) diagram of Pearce et al. [32]. (**b**) Binary Nb versus Y diagram of Pearce et al. [32]. (**c**) Binary discrimination K_2O/MgO versus 10,000*Ga/Al diagram of Whalen et al. [33]. (**d**) Binary discrimination Nb versus 10,000*Ga/Al diagram of Whalen et al. [33].

7.2. Petrogenesis of Homret El Gergab Alkali Feldspar Granite

The relationships between Rb, Sr, and Ba are helpful in inferring the origin of granites, either from partial melting or fractional crystallization. The K/Rb ratio is considered a good petrogenetic indicator that decreases during magmatic fractionation. K_2O concentration could reflect the enrichment of Rb in igneous rock types. K_2O versus Rb discrimination diagram shows that the alkali feldspar granite samples plot in the field of the Ras ed Dome ring complex, Sudan [37]. In addition, the analyzed granite samples plotted very closely to the pegmatitic-hydrothermal trend of Shaw [40] (Figure 13a), and some samples that deviated could be post-magmatic and/or auto-metasomatic alterations [41]. The behavior of these elements in granitic systems is strongly controlled by plagioclase, K-feldspar, and mica. A binary discrimination diagram of Rb versus Sr (Figure 13b) confirms the role

of K-feldspar fractionation in the studied granite. The average Ba/Rb ratio in the crust is approximately 4.4 [42]. Figure 13c shows that the studied granite samples occurred between 1 and 0.4 and are strongly enriched in Rb, which indicates the contribution of crustal material to the magmatic differentiation in the studied rock.

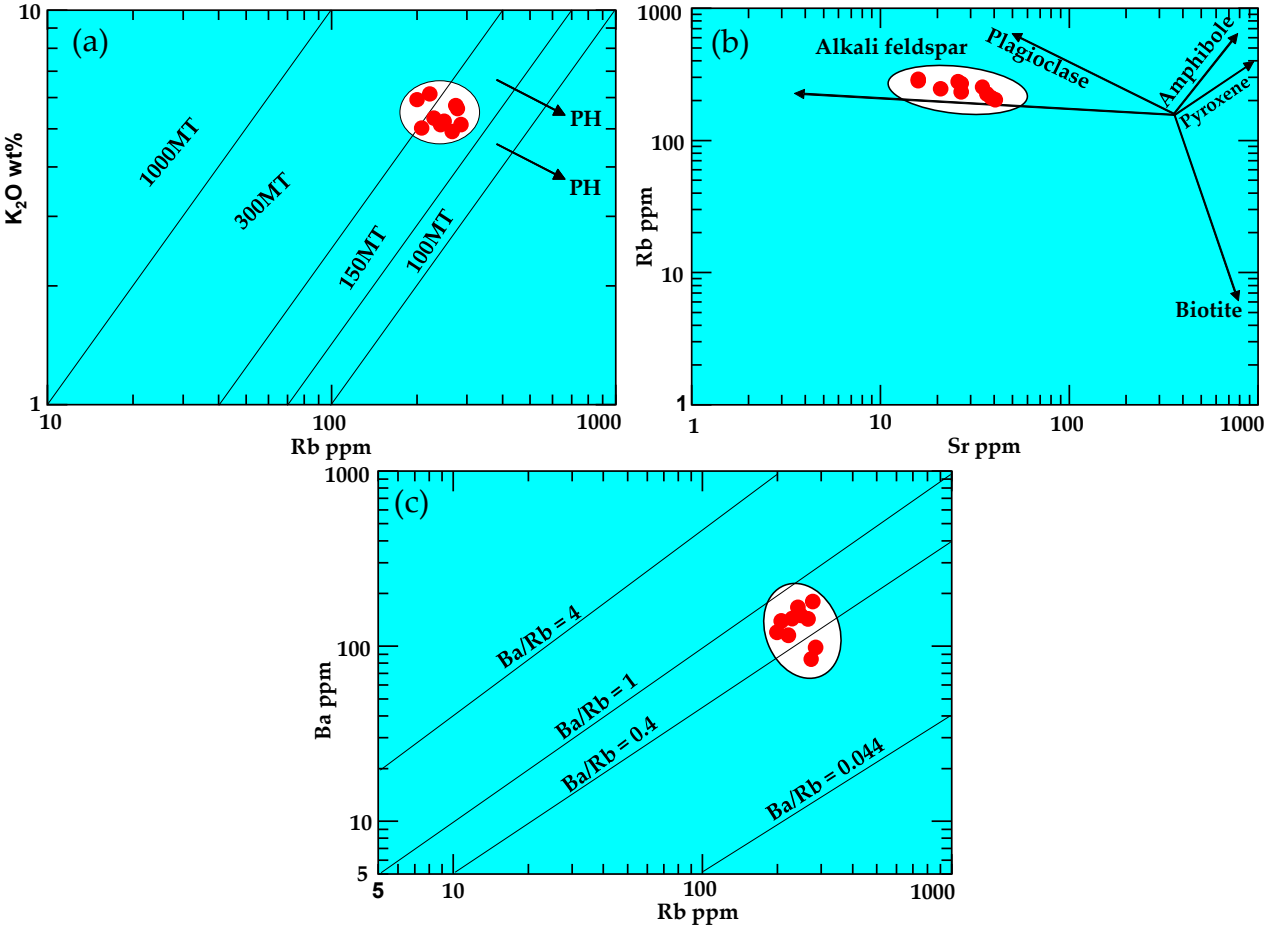

Figure 13. Petrogenesis discrimination diagrams show the distribution of the analyzed alkali feldspar granite samples. (**a**) Binary K_2O versus Rb diagram, where MT refers to the magmatic trend and PH refers to the pegmatitic hydrothermal trend, according to Shaw [40]. The shaded area illustrates the field of the Ras ed Dome ring complex, Sudan, according to O'Halloran [37]. (**b**) Binary Rb versus Sr diagram. (**c**) Binary Ba versus Rb diagram of Mason [42].

7.3. Zircon-Saturation Temperatures

The relationship between zircon solubility and the temperature of the melt is important for the Zr geothermometer. This approach could help determine the temperature and amount of Zr required for zircon formation in specific granite samples. Experimental research conducted by Watson and Harrison [43] on zircon saturation in various igneous rocks provides valuable data. The zircon saturation temperatures for the granite samples are listed in Table 1. The average estimated temperature for the alkali feldspar granite samples is close to 778 °C. The higher temperatures could suggest that the granite formed from a hotter magmatic source, potentially indicating the involvement of more evolved silica-rich melts. This could be crucial for understanding the most important conditions under which alkali feldspar granite has formed.

7.4. Insights into Rare Metals Mineralization

The enriched rare metal mineralization could being attributed to be crystallized from late magmatic melts. In addition, the higher concentrations of high-field strength elements (HFSEs) in the Homret El Gergab granite are considered good indicators of late-stage

differentiation. Thorite can be crystallized from a melt of Th-Y-Zr-rich silicate. Abdel-Karim [44] and Abdel Gawad [29] stated that during the progressive phase of magmatic crystallization, the residual melts of SiO_2 could have forced most of the monazite to crystallize in the early phase. Radioactive minerals such as uranothorite and thorite have been recorded in the investigated granite. They were of syngenetic origin during the emplacement of the alkali feldspar granite. The total oxide content of the analyzed uranothorite and thorite from alkali feldspar granite in the study area is approximately close to ~90 wt% (Tables 2 and 3), which could be related to the hydration processes and/or extensive metamictization [45,46]. Some thorite grains are spread in hematite (Figure 9b,e), which could indicate an extensive alteration. The presence of REEs in uranothorite and thorite could be related to their similarity in ionic radii compared to U and Th. This is responsible for allowing the REEs to occupy the same structural sites in these minerals. The crystallization of monazite may remove thorium from the residual melts, and the substitution in A-site could involve a marked replacement of P and REEs by Si and Th and/or replacement of REEs by Ca and Th as recorded by Williams et al. [47] as follows:

$$P^{5+} + REE^{3+} \leftrightarrow Si^{4+} + Th^{4+}$$

$$2REE^{3+} \leftrightarrow Ca^{2+} + Th^{4+}$$

It is important to know the relationship occurring between the metallogenitic stages of valuable rare metals mineralization. Nb-, Ta-rich minerals are often associated together, whereas Nb^{+5} and Ta^{+5} are very close to each other. Hydrothermal fluids rich in Nb and Ta could be responsible for the formation of columbite. The Ta/(Ta + Nb) ratios of the analyzed columbite spots ranged from 0.01 to 0.03, whereas the Mn/(Mn + Fe) ratios showed a much wider range, varying from 0.02 to 0.28 (Table 4). These ratios indicate a marked enrichment of iron in the analyzed columbite, revealing its typical ferrocolumbite composition according to Černý and Ercit [48].

Zircons are considered valuable carriers of rare metal ores such as Nb, Ta, Y, REEs, Hf, U, and Th. It is well noted that some thorite and xenotime grains occur in the form of fine grains along the rims of zircon crystals (Figures 9c,d and 10c,d). The spatial association of zircon with thorite and xenotime could suggest that they were crystallized from a highly fractionated fluid-rich magma. Additionally, xenotime (Y) is found in association with zircon and can vary in morphology from euhedral, igneous-like grains to irregular secondary grains formed by the dissolution of zircon in the presence of phosphorus-bearing fluids [49]. The average hafnium content in zircon (approximately 3.6; Table 5) is relatively higher than the normal value (approximately 1%). The presence of hafnium-rich zircons in the El Gergab granite is significant because it could be suggested that these rocks have undergone extensive differentiation and fractionation processes that occurred during their formation. This could be related to prolonged magma cooling and crystallization, as well as fractional crystallization [15]. EPMA data for zircons (Table 5) and their pleochroic halos indicate their enrichment in radioactive elements, especially U and Th. However, a detailed study of zircon grains revealed multistage zonation accompanied by changes in morphology. Some interstitial zircons associated with xenotime are evidence of subsequent formation by hydrothermal fluids (Figures 9 and 10). The presence of a combination of zircon, xenotime, and thorite could suggest an intermediate solid solution reaction, whereas the presence of zircon, columbite, and xenotime with anhedral habits could be related to the effect of fluorine on high-field strength elements, which increases their solubility [18].

Monazite and xenotime are the main sources of phosphatic-REE minerals. Igneous and hydrothermal monazite have been distinguished by their ThO_2 contents, vary from 3 to >5 wt% for igneous monazite and <1 wt% for hydrothermal ones [50]. The EPMA data show that the Th content is consistent with its igneous or magmatic origin (Table 6). Xenotime is considered the main source of Y and HREEs, and is distinguished by its Th concentration, which is similar to that of Cínovec granite [51].

7.5. Geodynamic Evolution

The geodynamic evolution of granites remains a subject of debate, and many studies have been conducted to understand the origin of different granitic rock types. Several petrogenetic schemes have been reconstructed to explain the origin of granites, including the following: (1) dehydration melting of tonalite-granodiorte rocks [52]; (2) fractional crystallization of basaltic magma that is derived from the mantle [53]; (3) partial melting of the residual sources after I-type granite extraction [33]; (4) low-pressure melting of the calc–alkaline magmas at the upper crust [54]; and (5) hybridization of the mantle-derived magmas with those of crustal melts [55].

In the ANS region, several models have been proposed in which A-type granites could originate from mantle derived magmas and the partial melting of the lower continental crust. In addition, extreme fractionation of the basaltic source magma has been proposed for A-type granites from El Ineigi [56]. In general, the lithospheric delamination process could have played a markedly useful role in the formation of A-type post-collision granite in response to the upwelling of asthenospheric magmas [20,39]. The heat required for partial melting can arise from various sources, and fluids such as water or carbon dioxide can lower the melting temperature of rocks, which could facilitate the partial melting processes. Once the magma forms, it could undergo further compositional changes during its ascent, contributing to the diversity of granites.

Figure 14 shows a simple petrogenetic model for the Homret El Gergab alkali feldspar A-type granite. This model suggests that the continental lithosphere underwent extension, resulting in upwelling, stretching, and thinning of both the mantle and crust. This model proposes the following: (1) The continental lithosphere underwent a markedly wide extension, which is responsible for the rising, stretching, and thinning of both the mantle and lower crust. This process is accompanied by basaltic magma injection, which is derived from the mantle into the continental lower crust. (2) The transfer of heat and fluids rich in volatiles percolation from basaltic magma into the continental lower crust could have led to a partial melting process of the lower crust materials. (3) The A-type granite could have resulted from the intrusion of the basaltic magma from the mantle into the lower crust [57–59].

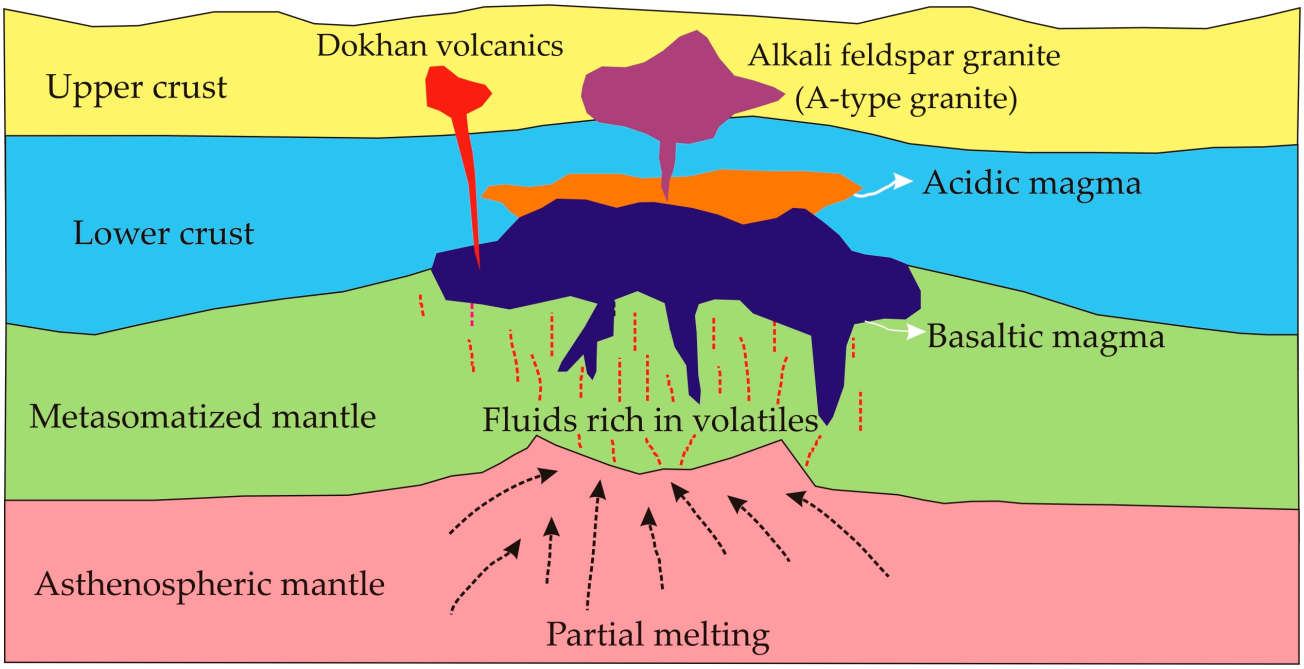

Figure 14. Simplified geodynamic model for the origin of the Homret El Gergab alkali feldspar granite modified after Tavakoli et al. [59].

8. Conclusions

Detailed petrological, geochemical, and mineralogical investigations indicate that the Homret El Gergab alkali feldspar granite is peraluminous, calc–alkaline series high-K, and emplaced within-plate environments. The alkali feldspar rare metal granite in the study area is distinguished by the higher content of alkali feldspar minerals, which form at higher temperatures and are more insoluble than others, indicating a greater degree of differentiation.

Mineralogical studies have identified various minerals, including uranothorite, thorite, columbite, zircon, monazite, and xenotime, as well as other accessory minerals. The close proximity of zircon to thorite and xenotime indicates that they could be formed from fluid-rich magmas and underwent a significant degree of fractionation.

Basaltic magmas play two main roles: (1) they supply the necessary heat to melt the Earth's crust, and (2) they provide volatile substances that seep into the lower continental layers, resulting in the formation of A-type granite by partial melting of the crust.

Author Contributions: Conceptualize, M.M.G., A.S.M. and A.E.A.G.; methodology, M.M.G., M.D., H.A.E.-D. and E.G.P.; software, M.M.G. and A.E.A.G.; validation, M.M.G., A.E.A.G., M.D., H.A.E.-D., E.G.P., A.S.M. and M.A.E.-L.; formal analysis, M.M.G. and E.G.P.; investigation, M.M.G., A.E.A.G., M.D., H.A.E.-D., E.G.P., A.S.M. and M.A.E.-L.; resources, M.M.G., M.D., H.A.E.-D., A.S.M. and M.A.E.-L.; data curation, A.E.A.G., M.M.G. and A.S.M.; Writing—original draft preparation: M.M.G., A.S.M. and A.E.A.G.; writing—review and editing, A.E.A.G., M.M.G. and A.S.M.; visualization, A.E.A.G., M.M.G., E.G.P., M.D., H.A.E.-D. and A.S.M.; supervision, M.M.G., E.G.P., A.E.A.G. and M.D.; funding acquisition, A.E.A.G. and E.G.P. All authors have read and agreed to the published version of the manuscript.

Funding: This research received no external funding.

Data Availability Statement: Data are contained within the article.

Conflicts of Interest: The authors declare no conflicts of interest.

References

1. Stern, R.J.; Hedge, C.E. Geochronologic and isotopic constraints on late Precambrian crustal evolution in the Eastern Desert of Egypt. *Am. J. Sci.* **1985**, *285*, 97–172. [CrossRef]
2. Liégeois, J.P.; Stern, R.J. Sr–Nd isotopes and geochemistry of granite–gneiss complexes from the Meatiq and Hafafit domes, Eastern Desert, Egypt: No evidence for pre-Neoproterozoic crust. *J. Afr. Earth Sci.* **2010**, *57*, 31–40. [CrossRef]
3. Helba, H.; Trumbull, R.B.; Morteani, G.; Khalil, S.O.; Arslan, A. Geochemical and petrographic studies of Ta mineralization in the Nuweibi albite granite complex, Eastern Desert, Egypt. *Miner. Depos.* **1997**, *32*, 164–179. [CrossRef]
4. Abu El-Rus, M.A.; Mohamed, M.A.; Lindh, A. Mueilha rare metals granite, Eastern Desert of Egypt: An example of a magmatic-hydrothermal system in the Arabian- Nubian Shield. *Lithos* **2017**, *294*, 362–382. [CrossRef]
5. Abuamarah, B.A.; Azer, M.K.; Asimow, P.D.; Ghrefat, H.; Mubarak, H.S. Geochemistry and petrogenesis of late Ediacaran rare-metal albite granites of the Arabian-Nubian Shield. *Acta Geol. Sin.* **2021**, *95*, 459–480. [CrossRef]
6. Abdel Gawad, A.E.; Skublov, S.G.; Levashova, E.V.; Ghoneim, M.M. Geochemistry and U–Pb Age dating of zircon as a petrogenetic tool for magmatic and hydrothermal processes in Wadi Ras Abda Syenogranite, Eastern Desert, Egypt. *Arab. J. Sci. Eng.* **2021**, *47*, 7351–7365. [CrossRef]
7. Skublov, S.G.; Abdel Gawad, A.E.; Levashova, E.V.; Ghoneim, M.M. U–Pb geochronology, REE and trace element geochemistry of zircon from El Fereyid monzogranite, south Eastern Desert, Egypt. *J. Miner. Pet. Sci.* **2021**, *116*, 220–233. [CrossRef]
8. Ghoneim, M.M.; Panova, E.G.; Abdel Gawad, A.E.; Yanson, S.Y. Morphological and geochemical features of zircon from intrusive rocks of El Sela area, Eastern Desert, Egypt. *N. Ural. State Min. Univ.* **2020**, *3*, 7–18. [CrossRef]
9. Surour, A.A.; Omar, S.A.M. Historiography and FTIR spectral signatures of beryl crystals from some ancient Roman sites in the Eastern Desert of Egypt. *Environ. Earth Sci.* **2020**, *79*, 520. [CrossRef]
10. Ali, M.A.; Abdel Gawad, A.E.; Ghoneim, M.M. Geology and mineral chemistry of uranium and thorium bearing minerals in rare-metal (NYF) pegmatites of Um Solimate, South Eastern Desert of Egypt. *Acta Geol. Sin.* **2021**, *95*, 1568–1582. [CrossRef]
11. Ghoneim, M.M.; Panova, E.G.; Abdel Gawad, A.E. Natural radioactivity and geochemical aspects of radioactive mineralisation in El Sela, South Eastern Desert, Egypt. *Int. J. Environ. Anal. Chem.* **2023**, *103*, 2338–2350. [CrossRef]
12. Abdel Gawad, A.E.; Ene, A.; Skublov, S.G.; Gavrilchik, A.K.; Ali, M.A.; Ghoneim, M.M.; Nastavkin, A.V. Trace element geochemistry and genesis of beryl from Wadi Nugrus, South Eastern Desert, Egypt. *Minerals* **2022**, *12*, 206. [CrossRef]

13. Sami, M.; Osman, H.; Ahmed, A.F.; Zaky, K.S.; Abart, R.; Sanislav, I.V.; Abdelrahman, K.; Fnais, M.S.; Xiao, W.; Abbas, H. Magmatic Evolution and Rare Metal Mineralization in Mount El-Sibai Peralkaline Granites, Central Eastern Desert, Egypt: Insights from Whole-Rock Geochemistry and Mineral Chemistry Data. *Minerals* **2023**, *13*, 1039. [CrossRef]
14. Alekseev, V.I.; Alekseev, I.V. The Presence of Wodginite in Lithium–Fluorine Granites as an Indicator of Tantalum and Tin Mineralization: A Study of Abu Dabbab and Nuweibi Massifs (Egypt). *Minerals* **2023**, *13*, 1447. [CrossRef]
15. Abdalla, H.M.; Helba, H.; Matsueda, H. Chemistry of zircon in rare metal granitoids and associated rocks, Eastern Desert, Egypt. *Resour. Geol.* **2009**, *59*, 51–68. [CrossRef]
16. Abdallah, S.E.; Azer, M.K.; El Shammari, A.S. The Petrological and geochemical evolution of Ediacaran rare-metal bearing A-type granites from Jabal Aja complex, northern Arabian Shield, Saudi Arabia. *Acta Geol. Sin. Engl. Ed.* **2020**, *94*, 743–762. [CrossRef]
17. Abdelkader, M.A.; Watanabe, Y.; Shebl, A.; El-Dokouny, H.A.; Dawoud, M.; Csámer, Á. Effective delineation of rare metal-bearing granites from remote sensing data using machine learning methods: A case study from the Umm Naggat Area, Central Eastern Desert, Egypt. *Ore Geol. Rev.* **2022**, *1*, 105184. [CrossRef]
18. Abdel-Azeem, M.M. Genesis of the rare metals mineralization in Um Safi acidic volcanics, Central Eastern Desert, Egypt. *Appl. Earth Sci.* **2024**, *30*, 25726838231225051.
19. Basta, E.Z.; Kotb, H.; Awadalla, M.F. Petrochemical and geochemical characteristics of the Dokhan Formation at the type locality, Jabal Dokhan, Eastern Desert, Egypt. *Inst. Appl. Geol. Jeddah Bull.* **1980**, *3*, 121–140.
20. Eliwa, H.A.; El-Bialy, M.Z.; Murata, M. Edicaran postcollisional volcanism in the Arabian-Nubian Shield: The high-K calc-alkaline Dokhan Volcanics of Gabal Samr El-Qaa (592 ± 5 Ma), North Eastern Desert, Egypt. *Precambrian Res.* **2014**, *246*, 180–207. [CrossRef]
21. Khamis, H.A.; El-Bialy, M.; Hamimi, Z.; Afifi, A.; Abdel Wahed, S.A. Petrographic investigation of the Precambrian basement rocks of Esh El Mallaha area, North Eastern Desert, Egypt. *Alfarama J. Basic Appl. Sci.* **2023**, *4*, 340–354.
22. Abd El-Hadi, A.M. Mineralogical and Geochemical Prospection and Radioelements Distribution in Hamrat Al Jirjab Stream Sediments, Esh El Melaha Range, North Eastern Desert, Egypt. Ph.D. Thesis, Faculty of Science, Benha University, Benha, Egypt, 2013; 251p.
23. Barker, F. Trondhjemite: Definition, environment and hypotheses of origin. In trondhjemites, dacites, and related rocks. *Dev. Petrol.* **1979**, *6*, 1–12.
24. Middlemost, E.A.K. Naming materials in the magma/igneous rock system. *Earth Sci. Rev.* **1994**, *37*, 215–224. [CrossRef]
25. Sun, S.S.; McDonough, W.F. Chemical and isotopic systematics of oceanic basalts: Implications for mantle composition and processes. In *Magmatism in Ocean Basins*; Saunders, A.D., Norry, M.J., Eds.; Geological Society London Special Publications: London, UK, 1989; Volume 42, pp. 313–345.
26. Taylor, S.R.; McLennan, S.M. Chemical composition and element distribution in the Earth's crust. *Encycl. Phys. Sci. Technol.* **2001**, *312*, 697–719.
27. Watt, G.R. High-thorium monazite-(Ce) formed during disequilibrium melting of metapelites under granulite-facies conditions. *Min. Mag.* **1995**, *59*, 735–743. [CrossRef]
28. Abd El Ghaffar, N.I. Enrichment of rare earth and radioactive elements concentration in accessory phases from alkaline granite, South Sinai- Egypt. *J. Afr. Earth Sci.* **2018**, *147*, 393–401. [CrossRef]
29. Abdel Gawad, A.E. Mineral chemistry (U, Th, Zr, REE) in accessory minerals from Wadi Rod Elsayalla granitoids, South Eastern Desert, Egypt. *Arab. J. Geosci.* **2021**, *14*, 1996. [CrossRef]
30. Maniar, P.D.; Piccoli, P.M. Tectonic discrimination of granitoids. *Geol. Soc. Am. Bull.* **1989**, *101*, 635–643. [CrossRef]
31. Rickwood, P.C. Boundary line within petrologic diagrams which use oxides of major and minor elements. *Lithos* **1989**, *22*, 247–263. [CrossRef]
32. Pearce, J.A.; Harris, N.B.W.; Tindle, A.G. Trace element discrimination diagrams for the tectonic interpretation of granitic rocks. *J. Petrol.* **1984**, *25*, 956–983. [CrossRef]
33. Whalen, J.B.; Currie, K.L.; Chappell, B.W. A-type granites: Geochemical characteristics, discrimination and petrogenesis. *Contrib. Min. Petrol.* **1987**, *95*, 407–419. [CrossRef]
34. Qiu, J.T.; Qiu, L. Geochronology and magma oxygen fugacity of Ehu S-type granitic pluton in Zhe-Gan-Wan region, SE China. *Geochemistry* **2016**, *76*, 441–448. [CrossRef]
35. Qiu, L.; Yan, D.P.; Zhou, M.F.; Arndt, N.T.; Tang, S.L.; Qi, L. Geochronology and geochemistry of the Late Triassic Longtan pluton in South China: Termination of the crustal melting and Indosinian orogenesis. *Int. J. Earth Sci. (Geol. Rundsch)* **2013**, *103*, 649–666. [CrossRef]
36. Qiu, L.; Li, X.; Li, X.; Yan, D.P.; Ren, M.; Zhang, L.; Cheng, G. Petrogenesis of early cretaceous intermediate to felsic rocks in Shanghai, South China: Magmatic response to Paleo-Pacific plate subduction. *Tectonophysics* **2022**, *838*, 229469. [CrossRef]
37. O' Halloran, D.A. Ras ed Dom migrating complex: A-type granites and syenites from the Bauda Desert, Sudan. *J. Afr. Earth Sci.* **1985**, *3*, 61–75.
38. Abdel Gawad, A.E.; Eliwa, H.; Ali, K.G.; Alsafi, K.; Murata, M.; Salah, M.S.; Hanfi, M.Y. Cancer Risk Assessment and Geochemical Features of Granitoids at Nikeiba, Southeastern Desert, Egypt. *Minerals* **2022**, *12*, 621. [CrossRef]
39. Khedr, M.Z.; Khashaba, S.M.; El-Shibiny, N.H.; Takazawa, E.; Hassan, S.M.; Azer, M.K.; Whattam, S.A.; El-Arafy, R.A.; Ichiyama, Y. Integration of remote sensing and geochemical data to characterize mineralized A-type granites, Egypt: Implications for origin and concentration of rare metals. *Int. J. Earth Sci.* **2023**, *112*, 1717–1745. [CrossRef]

40. Shaw, I.; Bunbury, J.A. Petrological Study of the Emerald Mines in the Egyptian Eastern Desert. In *Lthics at the Millannium*; Moloney, N., Shott, M.J., Eds.; Archaeopress: London, UK, 2003; pp. 203–213.
41. Vidal, P.; Dosso, L.; Bowden, P.; Lameyre, J. Strontium isotope geochemistry in syenite-alkaline granite complexes. In *Origin and Distribution of the Elements (2nd Symposium)*; Ahrens, L.H., Ed.; Pergamon Press: Oxford, UK, 1979; pp. 223–231.
42. Mason, B. *Principles of Geochemistry*, 3rd ed.; John Wiely: New York, NY, USA, 1966; 310p.
43. Watson, E.B.; Harrison, T.M. Zircon saturation revisited: Temperature and composition effects in a variety of crustal magma types. *Earth Planet. Sci. Lett.* **1983**, *64*, 295–304. [CrossRef]
44. Abdel-Karim, A.M. REE-rich accessory minerals in granites from southern Sinai, Egypt: Mineralogy, geochemistry and petrogenetic implications. In Proceedings of the 4th International Conference on Geochemistry, Bab Sharqi, Egypt, 15–16 September 1999; pp. 83–100.
45. Abd El-Naby, H.H. High and low temperature alteration of uranium and thorium minerals, Um Ara granites, south Eastern Desert, Egypt. *Ore Geol. Rev.* **2009**, *35*, 436–446. [CrossRef]
46. Abdel Gawad, A.E.; Ghoneim, M.M.; El-Taher, A.; Ramadan, A.A. Mineral chemistry aspects of U-, Th-, REE-, Cu-bearing minerals at El-Regeita shear zone, South Central Sinai, Egypt. *Arab. J. Geosci.* **2021**, *14*, 1–13. [CrossRef]
47. Williams, M.L.; Jercinovic, M.J.; Hetherington, C.J. Microprobe monazite geochronology: Understanding geologic processes by integrating composition and chronology. *Annu. Rev. Earth Planet Sci.* **2007**, *35*, 137–175. [CrossRef]
48. Černý, P.; Ecrit, T.S. Some recent advances in the mineralogy and geochemistry of Nb and Ta in rare-element granitic pegmatites. *Bull. Min.* **1985**, *108*, 499–532. [CrossRef]
49. Xie, L.W.; Yang, J.H.; Yin, Q.Z.; Yang, Y.H.; Liu, J.B.; Huang, C. High spatial resolution in situ U–Pb dating using laser ablation multiple ion counting inductively coupled plasma mass spectrometry (LA-MIC-ICP-MS). *J. Anal. At. Spectrom.* **2017**, *32*, 975–986. [CrossRef]
50. Schandl, E.S.; Gorton, M.P. A textural and geochemical guide to the identification of hydrothermal monazite: Criteria for selection of samples for dating epigenetic hydrothermal ore deposits. *Econ. Geol.* **2004**, *99*, 1027–1035. [CrossRef]
51. Johan, Z.; Johan, V. Accessory minerals of the Cínovec (Zinnwald) granite cupola, Czech Republic: Indicators of petrogenetic evolution. *Min. Petrol.* **2005**, *83*, 113–150. [CrossRef]
52. King, P.L.; White, A.J.R.; Chappell, B.W.; Allen, C.M. Characterization and origin of aluminous A-type granites from the Lachlan Fold Belt, southeastern Australia. *J. Petrol.* **1997**, *38*, 371–391. [CrossRef]
53. Christiansen, E.H.; Best, M.G.; Radebaugh, J. The origin of magma on planetary bodies. *Planet. Volcanism Across Sol. Syst.* **2022**, *1*, 235–270.
54. Skjerlie, K.P.; Johnston, A.D. Vapor-absent melting at 10 kbar of a biotite-and amphibole-bearing tonalitic gneiss: Implications for the generation of A-type granites. *Geology* **1992**, *20*, 263–266. [CrossRef]
55. Yang, J.H.; Wu, F.Y.; Wilde, S.A.; Xie, L.W.; Yang, Y.H.; Liu, X.M. Tracing magma mixing in granite genesis: In situ U–Pb dating and Hf-isotope analysis of zircons. *Contrib. Min. Petrol.* **2007**, *153*, 177–190. [CrossRef]
56. Mohamed, F.H.; El-Sayed, M.M. Postorogenic and anorogenic A-type fluorite-bearing granitoids, Eastern Desert, Egypt: Petrogenetic and geotectonic implications. *Geochemistry* **2008**, *68*, 431–450. [CrossRef]
57. Annen, C.; Sparks, R.S. Effects of repetitive emplacement of basaltic intrusions on thermal evolution and melt generation in the crust. *Earth Planet. Sci. Lett.* **2002**, *203*, 937–955. [CrossRef]
58. Abd El-Fatah, A.A.; Surour, A.A.; Azer, M.K.; Madani, A.A. Integration of Whole-Rock Geochemistry and Mineral Chemistry Data for the Petrogenesis of A-Type Ring Complex from Gebel El Bakriyah Area, Egypt. *Minerals* **2023**, *13*, 1273. [CrossRef]
59. Tavakoli, N.; Shabanian, N.; Davoudian, A.R.; Azizi, H.; Neubauer, F.; Asahara, Y.; Bernroider, M.; Lee, J.K. A-type granite in the Boein-Miandasht Complex: Evidence for a Late Jurassic extensional regime in the Sanandaj-Sirjan Zone, western Iran. *J. Asian Earth Sci.* **2021**, *213*, 104771. [CrossRef]